nature communications

Article

https://doi.org/10.1038/s41467-025-65689-w

Mitochondria relay cholesterol signal exacerbates osteoarthritis in mice

Received: 3 July 2025

Accepted: 21 October 2025

Yiyang Ma[1,2,7], Yidan Pang[1,2,7], Chenglong Liu[1,2,7], Yuchen Tian[1,2,7], Kaiwen Zheng[1,2], Meng Yao[1,2], Xiaofeng Liu[3], Ruomu Cao[4], Yiwei Zhao[4], Zhikai Zheng[1,2], Weitao Jia[1,2], Daoyu Zhu[1], Hao Peng[1], Dajiang Du[1], Xinhua Qu[5], Chuan-ju Liu[6], Pei Yang[4] ✉, Yigang Huang[1,2] ✉, Changqing Zhang[1,2] ✉ & Junjie Gao[1,2] ✉

Osteoarthritis (OA) is the most common joint disease characterized by joint inflammation and cartilage deterioration. Though disrupted cholesterol metabolism has been implicated in the pathogenesis of OA, the underlying mechanisms remains unclear. Here we demonstrate that increased cholesterol in joint is a crucial activator of the cGAS-STING pathway in cartilage during OA. Subchondral osteocytes, which contact with blood vessel and cartilage, increase their uptake of cholesterol and transfer mitochondria to cartilage to trigger its inflammatory pathway. This process is mediated by increased cytosolic mitochondrial DNA (mtDNA) in chondrocytes, and is further amplified through enhanced mitochondrial transfer between chondrocytes. Mechanistically, we identify a mitochondrial subpopulation in osteocytes that enriched in Nudt8, which act as a key regulator of metabolic-inflammatory crosstalk. Nudt8 alters cholesterol metabolism by degrading coenzyme A, leading to an accumulation of cytosolic mtDNA and subsequent activation of the cGAS-STING pathway in chondrocytes. Pharmacological targeting osteocyte mitochondrial Nudt8 by supplementing pantethine ameliorate inflammation in cartilage and joint pain in OA mice, offering a potential therapeutic strategy for OA.

Osteoarthritis (OA) is a degenerative whole-joint disease primarily characterized by deterioration of cartilage matrix[1,2] and joint inflammation, with clinical manifestations, such as pain and limited mobility that seriously affect the patient's ability to work and quality of life[3], though the etiology remains unclear. Recent evidence suggests that OA is associated with metabolic disorders, such as hypercholesterolemia[4,5], with clinical cohort evidence demonstrate that hypercholesterolemia may be an independent risk factor for OA[6–8] and high-cholesterol diet in animal model led to increased cartilage damage and OA severity[9–11]. However, the underlying molecular mechanism of cholesterol metabolism involved in OA pathogenesis still remains unclear that needs to be further explored.

Metabolic disorders are closely related to chronic inflammation[12,13], which is mediated primarily by the innate immune system[14], and play a

---

[1]Department of Orthopaedic Surgery, Shanghai Sixth People's Hospital Affiliated to Shanghai Jiao Tong University School of Medicine, Shanghai, China. [2]Institute of Microsurgery on Extremities, and Department of Orthopedic Surgery, Shanghai Sixth People's Hospital Affiliated to Shanghai Jiao Tong University School of Medicine, Shanghai, China. [3]Department of Orthopaedic Surgery, Shanghai Sixth People's Hospital Fujian, Quanzhou, Fujian, China. [4]Department of Bone and Joint Surgery, the Second Affiliated Hospital of Xi'an Jiaotong University, Xi'an, Shanxi, China. [5]Department of Bone and Joint Surgery, Renji Hospital, Shanghai Jiaotong University School of Medicine, Shanghai, China. [6]Department of Orthopaedics and Rehabilitation, Yale University School of Medicine, New Haven, CT, USA. [7]These authors contributed equally: Yiyang Ma, Yidan Pang, Chenglong Liu, Yuchen Tian. ✉e-mail: yangpei@xjtu.edu.cn; yiganghuang@sjtu.edu.cn; zhangcq@sjtu.edu.cn; colingjj@163.com

critical role in OA pathogenesis. Inflammatory mediators can induce the expression of matrix-degrading enzymes of chondrocytes, leading to cartilage destruction. Besides, OA chondrocytes could secrete proinflammatory cytokines[15], together with the damage-associated molecular patterns released during cartilage erosion[16], contributing to inflammation exacerbation. However, the mechanism by which cholesterol triggers and amplifies inflammatory signals within cartilage remains elusive.

Mitochondria are central to regulating both cell metabolism and inflammation through various mechanisms. They are known as the organelles for production of respiratory ATP and play essential roles in regulating various metabolic process[17,18] and innate immune response[19]. Beyond maintaining cellular homeostasis, intercellular mitochondrial transfer has recently emerged as a mechanism for crosstalk in tissue signaling, which is critically involved in modulating the pathogenesis of numerous diseases[20–22]. Here, we show that the subchondral osteocytes, which contact with blood vessel and cartilage, increase their uptake of cholesterol and transfer mitochondria via intercellular nanotubes to cartilage, which subsequently amplifies the activation of cGAS-STING pathway in cartilage, and accelerate OA progression. We further demonstrated that osteocyte mitochondrial Nudt8 prompts cholesterol and inflammatory crosstalk in chondrocytes. Targeting the transfer of osteocyte mitochondria by supplementing pantethine could ameliorate OA severity.

Results

Cholesterol induces inflammation by activating cGAS-STING pathway in cartilage during OA

We analyzed published single-cell RNA-seq data[23] and found that the cholesterol metabolism was disrupted in human cartilage at the late stage of OA (Fig. S1a). Using filipin staining for detection of cholesterol, we found that cartilage was under an excessive cholesterol burden in OA patient (Fig. 1a) and destabilization of the medial meniscus (DMM) induced post-traumatic OA (PTOA) mouse model on normal chow (Fig. 1b), indicating disordered cholesterol metabolism involved in OA pathogenesis. Though the involvement of cholesterol metabolic pathway in cartilage degeneration and OA pathogenesis has been reported[11], its relationship with joint inflammatory signals within cartilage remains elusive. To study this, we employed high-cholesterol diet (HCD) in mice and subjected them to DMM surgery. In comparison with regular diet (RD) group, both male and female mice in HCD group exhibited increased serum low-density lipoprotein cholesterol (LDL-C) levels (Fig. S1b), and filipin staining confirmed elevated cholesterol in cartilage after 7-week HCD feeding (Fig. S1c). In comparing RD-OA male mice with HCD-OA male mice, gait analysis revealed that HCD-OA groups exhibited a significant increase in swing/stance ratio along with a decrease in both average pressure and maximal pressure (Figs. 1c and S1d). Histological assessments indicated more severe cartilage damage in HCD-OA male mice with significantly higher OARSI score (Fig. 1d) and more severe synovitis (Fig. 1e). HCD OA female mice exhibited same phenotypes seen in male mice with no apparent sex differences were observed (Fig. S1e–h). These changes suggested that HCD exacerbated OA severity in both male and female mice. To explore the possible association of cholesterol with inflammatory signals in cartilage, we harvested articular cartilage from HCD-OA mice under microscope. Protein expression analysis by western blotting revealed that NF-κB pathway, which plays vital inflammatory role in chondrocytes, were activated in cartilage of HCD-OA mice (Fig. S1i, j). NF-κB pathway could be mainly activated by innate immune responses, including cGAS-STING pathway[24,25]. We then validated the activation of the cGAS-STING pathway in cartilage from OA patients (Figs. 1f and S1k), and DMM mice (Figs. 1g and S1l), which was further aggravated in the cartilage from HCD OA mice, accompanied with elevated levels of MMP3 and MMP13 (Figs. 1h and S1m, n), demonstrating cholesterol activated the cGAS-STING pathway in cartilage.

To study the role of cholesterol-activated cGAS-STING pathway in cartilage, we treated HCD-OA mice with STING inhibitor (H-151)[26] by intra-articular injections. Through several behavioral tests, such as gait analysis for assessing weight-bearing asymmetry (Fig. S2a), open field test for assessing movement activity (Fig. S2b, c) and von Frey test for assessing inflammatory microenvironment induced mechanical allodynia (Fig. S2d), a significant pain reduction was observed in H-151-treated HCD-OA mice. Histological analysis revealed preserved articular cartilage structure and maintained proteoglycan content (Fig. S2e) and ameliorated synovitis (Fig. S2f, g) in HCD-OA mice treated with H-151, with no apparent sex difference (Fig. S2h–m). Although we use HCD model to exacerbate cholesterol accumulation in cartilage, OA itself can induce cholesterol elevation and subsequent cGAS-STING pathway activation even in RD model. Therefore, we established DMM model in RD mice to further validate the role of cGAS-STING pathway. In H-151-treated RD-OA mice, a significant pain reduction was observed through gait analysis (Figs. 1i and S2n), von Frey test (Fig. 1j) and open field test (Fig. 1k). Administration of H-151 in RD-OA mice yielded consistent histological improvements (Fig. 1l, m) and reduced synovitis (Fig. 1n). These beneficial effects were equally evident in both sexes (Fig. S2o–v), indicating a uniform therapeutic response regardless of gender. To investigate the specifically role of cGAS-STING pathway in cartilage, we generated DMM-induced PTOA mice in which cGAS is specifically deleted in chondrocytes (Col2a1^{ERT2}cGAS^{floxed} mice), and found that OA progression was ameliorated, as indicated by improved histological scores in both male (Fig. 1o) and female mice (Fig. S2i). Intriguingly, synovitis was ameliorated in Col2a1^{ERT2}cGAS^{floxed} mice when compared to Col2a1^{ERT2} mice (Figs. 1p and S2j), indicating that cGAS-STING pathway activation in cartilage could promote synovial inflammation in OA mice. Collectively, the findings from both model of STING inhibitor treatment and target deletion of cGAS suggest that cholesterol activated cGAS-STING pathway in cartilage contributes to OA progression.

Cholesterol triggers mitochondrial transfer via intercellular nanotubes to activate cGAS-STING pathway in chondrocytes

We then investigated whether cholesterol directly activates cGAS-STING pathway in chondrocytes. Surprisingly, we found 100 μM cholesterol treatments, which could induce metabolic perturbations in various cell types and trigger mRNA-level changes in chondrocytes[11,27] had no effects on either the cGAS-STING pathway molecules, such as phosphorylation of TBK1, IRF3, or the level of proinflammatory cytokine (*Il6 and IL1b*) in primary articular chondrocytes cultured under either normal condition (Fig. S3a–c) or IL-1β-mimic inflammatory environment in OA (Fig. S3d). We also examined mitochondrial energy metabolism since the damaged mitochondria is the major source of cytosolic DNA that closely related to cGAS-STING pathway activation[19], but found comparable oxidative phosphorylation level in cholesterol treated chondrocytes (Fig. S3e). These data suggest that cholesterol has no direct effect on chondrocyte mitochondrial homeostasis and downstream cGAS-SITNG pathway activation in vitro, prompting the possibility that the regulatory role of cholesterol in cartilage inflammation observed in vivo OA models could depend on the tissue crosstalk.

To explore this, we focused on the adjacent tissues. Articular cartilage is tightly anchored with subchondral bone to form the osteochondral unit[28]. Interestingly, we found that in the subchondral bone, osteocytes, the most important regulating cells embedded in the subchondral bone matrix, showed direct connection with chondrocytes via intercellular nanotubes (Fig. 2a). Further, filipin staining revealed elevated cholesterol level of osteocyte in OA patient and OA mice (Fig. 2b, c), as well as in HCD mouse model (Fig. S3f). Our previous results revealed that osteocytes, directly contact with blood vessels[29]—the main transport route of cholesterol[30]. Thus, we predicted that osteocyte could be the potential target of cholesterol in OA. Unlike

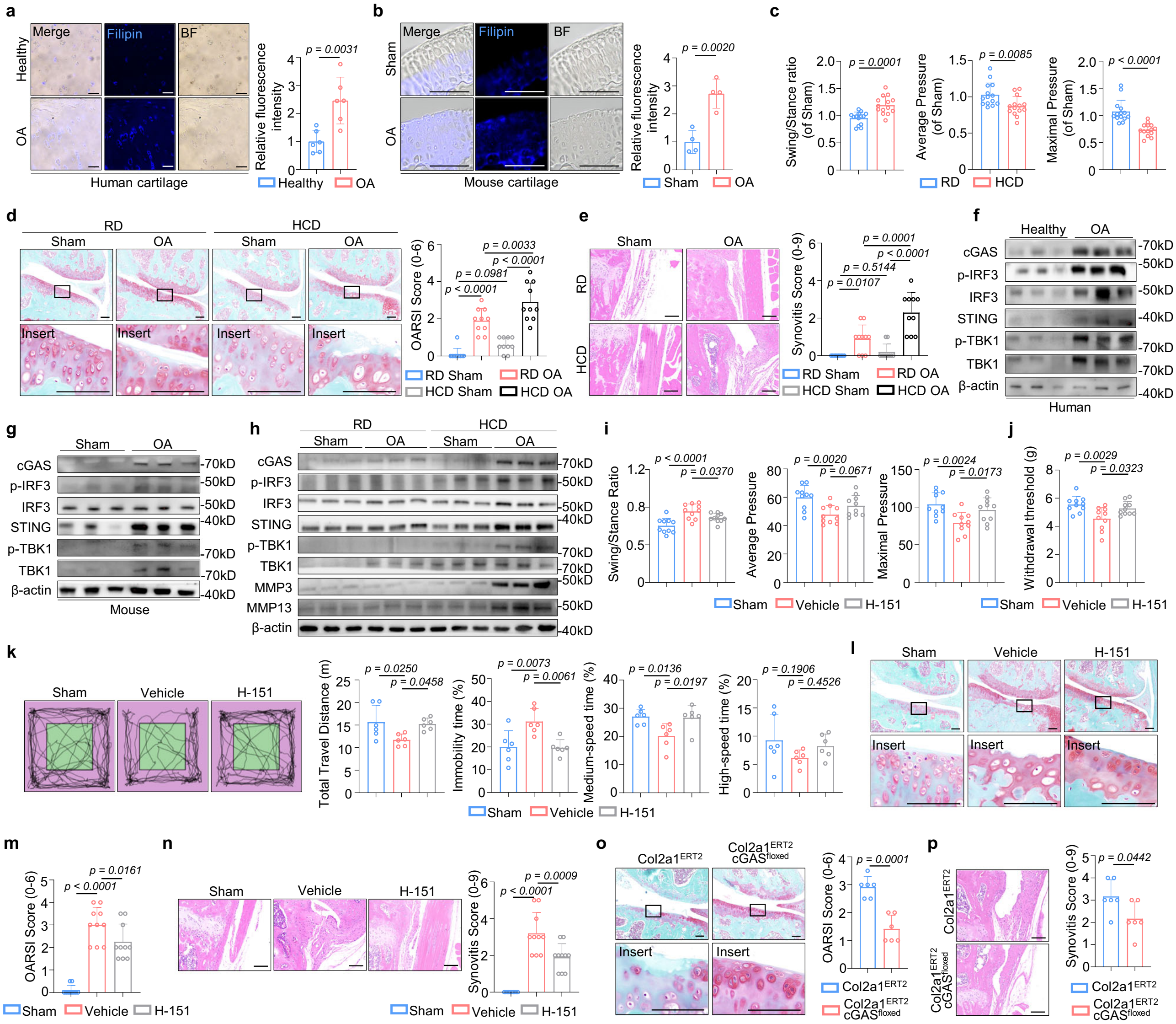

Fig. 1 | Cholesterol induces inflammation by activating cGAS-STING pathway in cartilage during OA. Filipin staining to detect cholesterol in **a** cartilage from humans with OA (n = 6 per group) and **b** cartilage from mice with OA (n = 4 per group). Scale bar: 100 µm. **c** Gait pattern quantitative results (n = 14 per group), **d** a representative image of safranin-O staining and OARSI score, **e** a representative image of H&E and synovitis score (n = 10 per group) of male HCD DMM mice. Scale bar: 100 µm. Western blot analysis of cGAS-STING pathway of **f** cartilage from humans with OA and **g** mice with OA. **h** Western blot analysis of cGAS-STING pathway and matrix-degrading enzymes of cartilage from HCD DMM mice. **i** Gait pattern quantitative results (n = 10 per group), **j** von Frey tests (n = 10 per group), **k** open field tests (n = 6 per group), **l** a representative image of safranin-O staining and **m** OARSI score, **n** a representative image of H&E and synovitis scores (n = 10 per group) of DMM model of male mice treated with H-151. Scale bar: 100 µm. **o** A representative image of safranin-O staining and OARSI scores, **p** a representative image of H&E and synovitis scores of DMM model of male Col2a1^{creER}cGAS^{floxed} mice (n = 6 per group). Scale bar: 100 µm. Data are presented as the mean ± SD, with biologically individual data points shown. *p* values were determined using unpaired two-tailed Student's *t* test (**a**–**c**, **o**, **p**), and one-way ANOVA with post hoc Šídák test (**d**, **e**, **i**–**n**). Source data are provided as a Source data file.

chondrocytes (Fig. S3e), the seahorse analysis revealed that cholesterol treatment impaired oxidative phosphorylation in mouse osteocyte cell line (Fig. S3g), indicating increased cholesterol in osteocytes during OA regulates osteocyte mitochondria. Our previous work revealed that osteocyte mitochondria, functioning as signal shuttles, could transfer via dendrites to regulate intercellular crosstalk[22,29,31,32]. Since we observed that in knee joint of mice, osteocytes directly connect to chondrocytes and endothelial cells via intercellular nanotubes, forming an endothelial cell-osteocyte-chondrocyte (EOC) structure (Fig. 2a), we hypothesize that osteocyte could transmit cholesterol signals by transferring mitochondria via intercellular nanotubes to chondrocytes. To tracing the transferring mitochondria, the green monomeric fluorescent protein Dendra2 was transfected into the mitochondria of the mouse osteocyte cell line to generate mouse osteocyte cell line expressing mitochondria-Dendra2 (mtD2-OY). We then co-cultured mtD2-OY with primary articular chondrocytes isolated from mT/mG mice-cell membrane was labeled with red fluorescence protein (mT-AC). By confocal imaging, we observed that intercellular nanotubes were formed between mT-AC and mtD2-OY, and green fluorescence mitochondria were observed in mT-AC (Fig. 2d). Further, by flow cytometry (FCM) analysis, mT-AC showed elevated green fluorescence when coculture with mtD2-Y4 (Fig. S3h), indicating the intercellular mitochondrial transfer. Supplementation with cytochalasin B (CyB), an inhibitor of nanotubes formation[33], could significantly downregulate this phenomenon (Fig. 2e), indicating the mitochondria from mtD2-OY were transferred to chondrocytes via intercellular nanotubes. To trace the osteocyte mitochondrial transfer in vivo, the Dmp1^{cre}PhAM^{floxed} mouse lineage was employed, in which

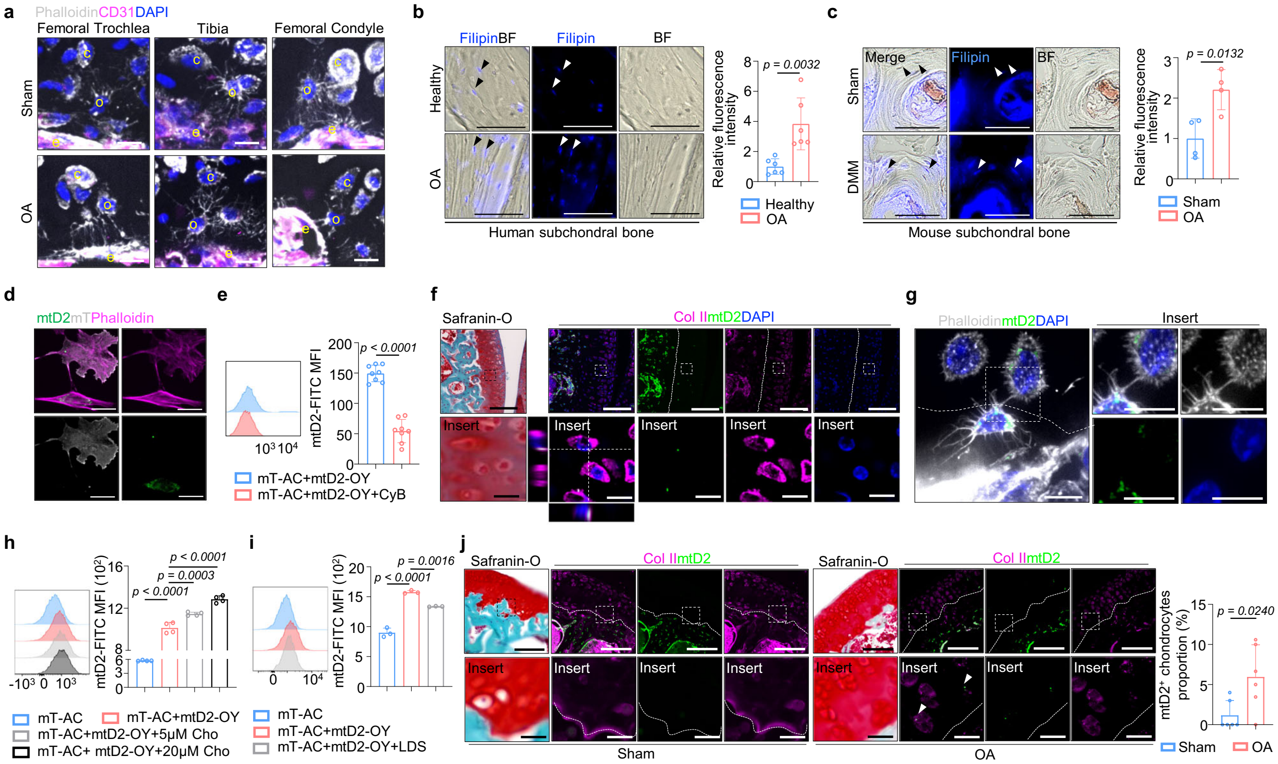

Fig. 2 | Cholesterol triggered mitochondrial transfer via intercellular nanotubes to chondrocytes. a Immunofluorescence of osteocyte contact with chondrocyte and endothelial cells in mice joint sample. o osteocyte, c chondrocyte; e endothelial cell. Scale bar: 20 µm. Filipin staining to detect cholesterol in **b** subchondral bone from humans with OA (n = 6 per group) and **c** subchondral bone from mice with OA (n = 4 per group) (arrow indicate osteocytes). Scale bar: 100 µm. **d** Immunofluorescence of mT-AC (gray signal) cocultured with mtD2-OY. Scale bar: 10 µm. **e** FCM analysis of FITC-A intensity of mT-AC cocultured with mtD2-OY treated with cytochalasin B (CyB) (n = 8 per group). **f** Representative safranin-O staining and immunostaining of cartilage of 10-week-old Dmp1^{cre} PhAM^{floxed} mice. Scale bar: 100 µm. Insert scale bar: 20 µm. **g** Representative immunostaining of subchondral osteocyte of 10-week-old Dmp1^{cre} PhAM^{floxed} mice. Scale bar: 20 µm. FCM analysis of FITC-A intensity of mT-AC cocultured with mtD2-OY under **h** cholesterol stimulation (n = 4 per group) and **i** lipid deficiency environment (n = 3 per group). LDS lipid deficiency serum. **j** Representative safranin-O staining and immunostaining of OA model of Dmp1^{cre} PhAM^{floxed} mice (n = 6 per group). Arrows indicate osteocyte mitochondria that inside the chondrocyte. Scale bar: 100 µm. Insert scale bar: 20 µm. Data are presented as the mean ± SD, with biologically individual data points shown. *p* values were determined using unpaired two-tailed Student's *t* test (**b**, **c**, **e**, **j**), and one-way ANOVA with post hoc Šídák test (**h**, **i**). Source data are provided as a Source data file.

the mitochondria of osteocytes were specifically labeled by Dendra2. We found the presence of osteocyte mitochondria in the cartilage, and orthogonal view of confocal image verified that several mtD2 signals are intracellular and localized within chondrocytes (Fig. 2f). Further, we focused on the EOC structure and demonstrated that osteocyte mitochondria were internalized within chondrocytes that contacted with osteocytes via intercellular nanotubes in healthy mice (Fig. 2g). To rule out the possibility that the fluorescence signals resulted from the migration of Dmp1^{+} cells or expression of Dmp1 in chondrocytes, we employed Dmp1^{cre}mG/mT mice, and the results revealed that there was no Dmp1^{+} cells in the cartilage (Fig. S3i). Given that the entire joint is under cholesterol burden during OA, we cocultured mT-AC (chondrocytes) and mtD2-OY (osteocytes) and supplemented with cholesterol (Fig. S3j) and found that mT-AC contained more mitochondria from mtD2-OY under excessive cholesterol conditions compared to control cocultures (Fig. 2h). In contrast, this phenomenon is significantly downregulated either by using CsB to inhibit nanotubes formation (Fig. S3k) or culturing mT-AC and mtD2-OY using lipid-deficiency serum (Fig. 2i). These results suggest that cholesterol triggers the transfer of osteocyte mitochondria to chondrocytes. To validate this finding in vivo, we subjected Dmp1^{cre}PhAM^{floxed} and Dmp1^{cre}mG/mT mice to DMM-induced PTOA model, in which cartilage and subchondral osteocytes were under cholesterol burden in OA. We observed there were more osteocyte mitochondria content in cartilage of OA joints (Fig. 2j), with Dmp1^{cre}mG/mT ruling out the migration of Dmp1^{+} cells into cartilage in DMM model (Fig. S3l), suggesting cholesterol could play an essential role in triggering the transfer of osteocyte mitochondria to chondrocytes.

To explore the function of transferred osteocyte mitochondria in chondrocytes, we isolated mitochondria from mouse osteocyte cell line (OY-Mito) and transplanted them into primary chondrocytes. Bulk RNA-seq analysis revealed that inflammatory-related pathways were enriched in chondrocytes receiving osteocyte mitochondria (Fig. 3a). In addition, cytosolic DNA sensing pathway was enriched in chondrocytes receiving osteocyte mitochondria as well (Fig. 3b). Mitochondria contained its own DNA (mtDNA) that could activate cytosolic DNA sensor. Subcellular fractionation assays (Fig. S4a, b) revealed that transplantation of osteocyte mitochondria significantly increased cytosolic mtDNA levels in chondrocytes (Fig. 3c). Subsequently, the cGAS-STING pathway was activated (Figs. 3d and S4c, d) and expression of genes related to downstream STING-dependent inflammation (*Ifit1, Irf7* and *Isg15*), proinflammatory cytokines (*Il1b* and *Il6*) as well as matrix-degrading enzymes (*Mmp3* and *Mmp13*) were upregulated (Figs. 3e and S4e). In contrast, knocking-down cGAS or STING in chondrocytes in vitro (Figs. 3f and S4f) significantly ameliorated osteocyte mitochondria-induced matrix degradation enzymes and inflammatory cytokines (Figs. 3f, g and S4f, g). Using STING inhibitor (H-151) to deactivate cGAS-STING pathway in chondrocyte cultures (Fig. S4h, i) also ameliorate osteocyte mitochondria-induced expression of genes related

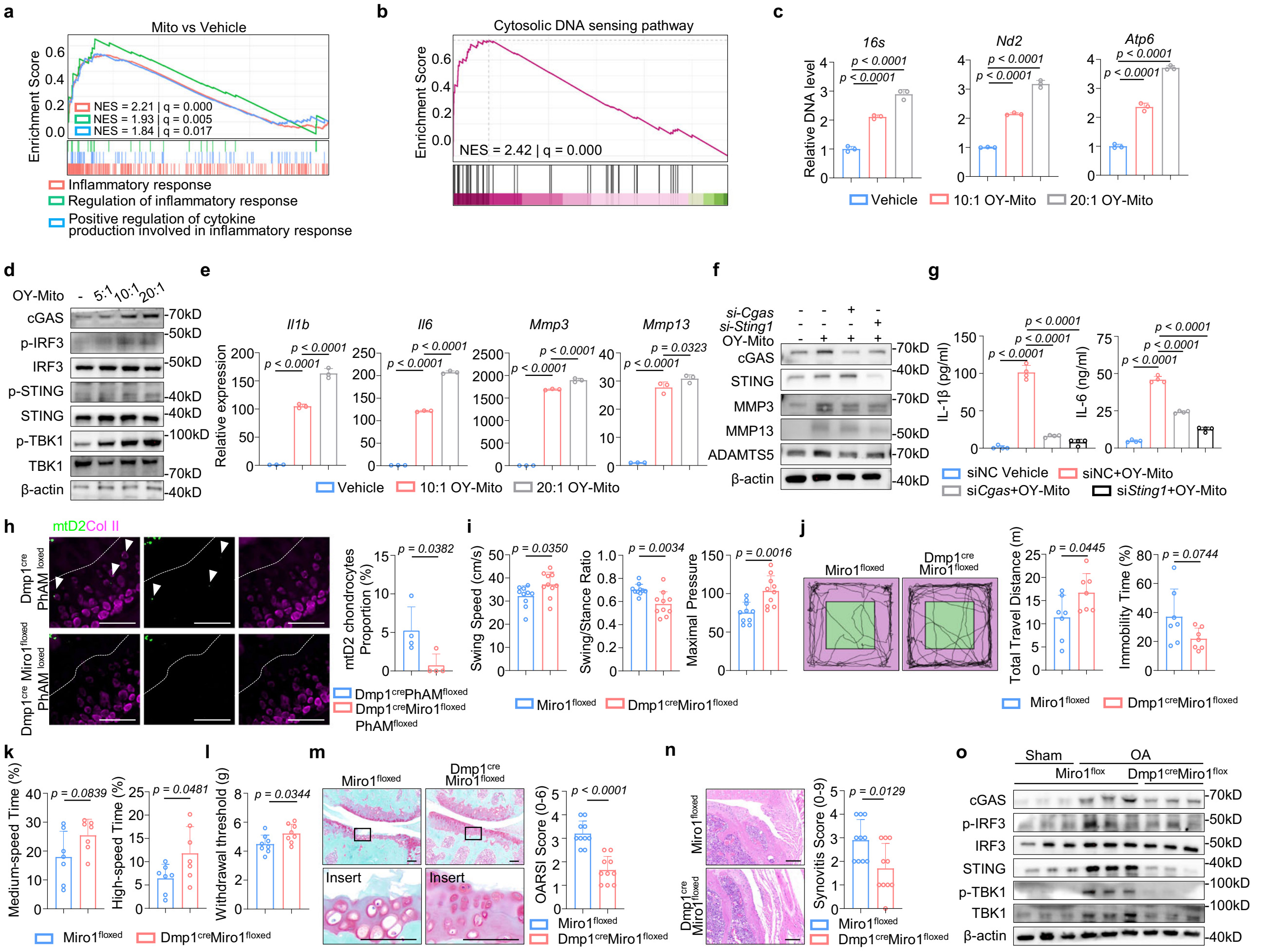

Fig. 3 | Osteocyte mitochondrial transfer activates cGAS-STING pathway in chondrocytes. GSEA analysis showing enrichment of **a** inflammatory pathway and **b** cytosolic DNA sensing pathway in chondrocytes after osteocyte mitochondrial transplantation. **c** Cytosolic mtDNA gene level (n = 3 per group), **d** Western blot analysis of cGAS-STING pathway and **e** mRNA level of genes related to proinflammatory cytokines and matrix-degrading enzymes of chondrocytes transplanted with osteocyte mitochondria (n = 3 per group). **f** Western blot analysis of cGAS-STING pathway and **g** cytokines in the supernatant of cGAS/STING knockdown chondrocytes transplanted with osteocyte mitochondria (n = 4 per group). **h** Representative immunostaining of cartilage of 10-week-old Dmp1^{cre}Miro1^{floxed}PhAM^{floxed} mice. Arrows indicate osteocyte mitochondria that inside the chondrocyte. Scale bar: 100 µm (n = 4 per group). **i** Gait pattern quantitative results (n = 10 per group), **j**, **k** open field tests (n = 7 per group), **l** von Frey tests (n = 8 per group), **m** a representative image of safranin-O staining and OARSI scores and **n** a representative image of H&E and synovitis scores (n = 10 per group) of male Dmp1^{cre} PhAM^{floxed} mice. Scale bar: 100 µm. **o** Western blot analysis of cGAS-STING pathway of cartilage from DMM model of Dmp1^{cre} PhAM^{floxed} mice. Data are presented as the mean ± SD, with biologically individual data points shown. *p* values were determined using unpaired two-tailed Student's *t* test (**h**–**n**), and one-way ANOVA with post hoc Šídák test (**c**, **e**, **g**). Source data are provided as a Source data file.

to downstream STING-dependent inflammation (*Ifit1, Irf7* and *Isg15*), proinflammatory cytokines (*Il1b* and *Il6*), matrix-degrading enzymes (*Mmp3* and *Mmp13*) (Fig. S4j, k). The matrix degradation enzymes (Fig. S4l) and inflammatory cytokines (Fig. S4m) induced by osteocyte mitochondria were also downregulated by H-151. In contrast, co-culturing chondrocytes with osteocytes via conditioned medium, which did not facilitate mitochondrial transfer to chondrocytes (Fig. S4n), did not activate the cGAS-STING pathway or induce matrix degradation (Fig. S4o), indicating that osteocyte-secreted factors have minimal effects, while mitochondrial transfer is necessary for osteocytes to exert their regulatory role. Collectively, these findings demonstrate that cholesterol transfer osteocyte mitochondria to activate the cGAS-STING pathway in chondrocytes.

Inhibiting osteocyte mitochondrial transfer attenuate OA progression or severity

To validate the role of osteocyte mitochondria in joint inflammation and cartilage deterioration, we first blocked mitochondrial transfer by knocking down Miro1[34] in mtD2-OY and confirmed there was less osteocyte mitochondrial transfer to chondrocytes when cocultured with mT-AC in vitro (Fig. S5a). Mice with knock-out Miro1 in osteocytes (Dmp1^{cre}Miro1^{floxed} mice) at 2- and 6-month-old ages showed no phenotypic changes in articular cartilage under normal conditions (Fig. S5b). We then generated Dmp1^{cre}Miro1^{floxed} PhAM ^{floxed} mice, and subjected them to DMM model and observed fewermtD2 signals in cartilage, indicating inhibited osteocyte-chondrocyte mitochondrial transfer (Fig. 3h). Further, in Dmp1^{cre}Miro1^{floxed} mice OA mouse model, we observed less impairment in gait pattern (Figs. 3i and S5c), improved open field movement activity (Fig. 3j, k), mild mechanical allodynia as indicated by the von Frey test OA Dmp1^{cre}Miro1^{floxed} mice (Fig. 3l). Histologically, OA Dmp1^{cre}Miro1^{floxed} mice showed reduced cartilage deterioration and synovitis compared to OA Miro1^{floxed} mice (Fig. 3m, n). No apparent sex difference was observed (Fig. S5d–i). Moreover, the activation of the cGAS-STING pathway in cartilage was significantly inhibited in OA Dmp1^{cre}Miro1^{floxed} mice (Figs. 3o and S5j). Collectively, these findings demonstrate that the transfer of osteocyte

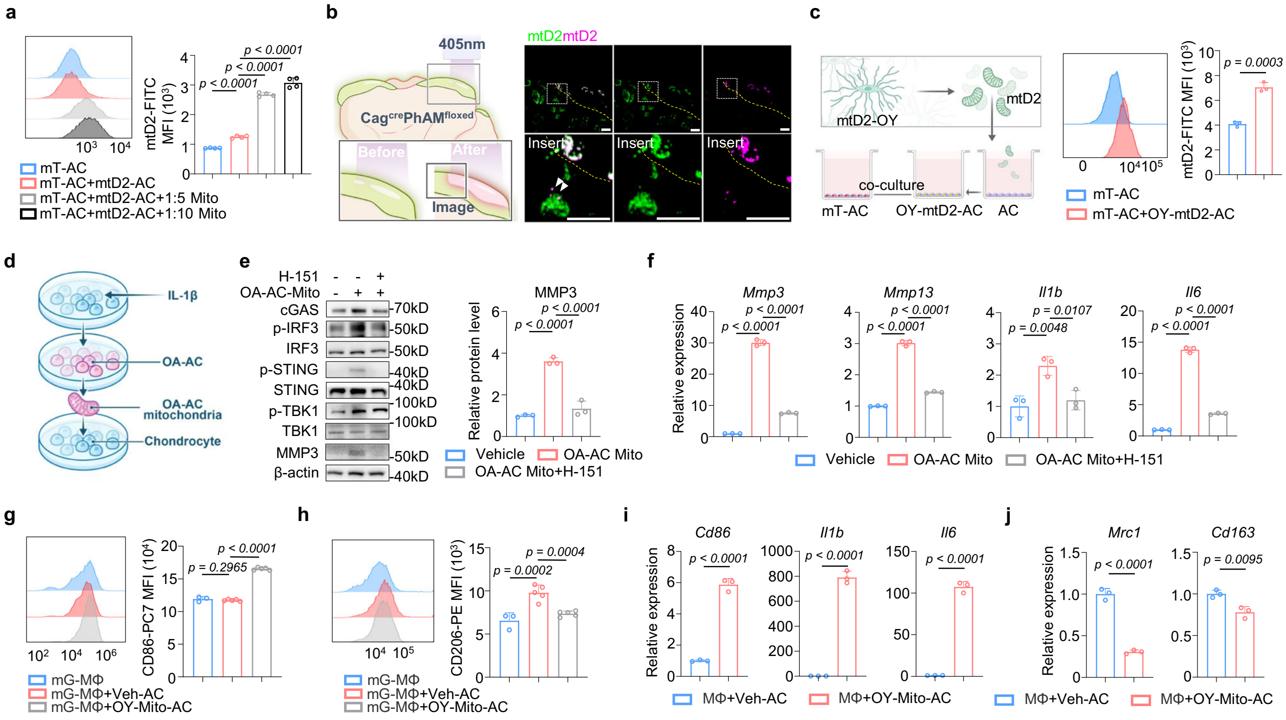

Fig. 4 | Osteocyte mitochondria amplify inflammation via triggering mitochondrial transfer between chondrocytes. a FCM analysis of FITC-A intensity of mT-AC cocultured with mtD2-OY under osteocyte mitochondria transplantation (n = 4 per group). **b** Schematic of photo-switching chondrocytes. Irradiation of the articular cartilage of the lateral tibial plateau with a 405-nm laser results in a photo-switch of green-mtD2 (green signal) to red-mtD2 (magenta signal). Confocal images of the photo-switched area in the lateral tibial plateau of Cag^{cre} PhAM^{floxed} mice cultured ex vivo for 2 days. Arrows indicate photo-switched mitochondria that inside the non-405-irradiated chondrocyte. Scale bar: 100 µm. **c** Schematic and FCM analysis of mT-AC cocultured with chondrocytes transplanted with mitochondria isolated from mtD2-OY (n = 3 per group). **d** Schematic and **e** western blot analysis of cGAS-STING pathway and **f** mRNA level of genes related to proinflammatory cytokines and matrix-degrading enzymes of chondrocytes transplanted with OA chondrocyte mitochondria and treated with H-151 (n = 3 per group). FCM analysis of **g** CD86 and **h** CD206 of mG-macrophage (mG-MΦ) cocultured with chondrocyte transplanted with osteocyte mitochondria (n = 3 for mG-MΦ group and n = 5 for coculture group). mRNA level of **i** M1 and **j** M2 related gene of macrophage cultured with conditioned medium of chondrocytes transplanted with osteocyte mitochondria (n = 3 per group). Data are presented as the mean ± SD, with biologically individual data points shown. *p* values were determined using unpaired two-tailed Student's *t* test (**c**, **i**, **j**), and one-way ANOVA with post hoc Šídák test (**a**, **e**–**h**). Source data are provided as a Source data file.

mitochondria ameliorates cartilage inflammation and joint degeneration during OA progression.

Osteocyte mitochondria amplify inflammation via triggering mitochondrial transfer between chondrocytes

We further studied how osteocyte mitochondria amplify inflammatory signals within cartilage. Given that chondrocytes within cartilage have the capacity to communicate through intercellular connections[35], and osteocyte mitochondria are present throughout the full thickness of cartilage (Fig. 2f), we hypothesized that osteocyte mitochondria could amplify inflammatory signals in cartilage via regulating mitochondrial transfer between chondrocytes. To verify this, we co-cultured chondrocytes containing mitochondria-Dendra2 (mtD2-AC) with mT-AC (chondrocytes). Using flow cytometry, we validated that intercellular mitochondrial transfer also occurs between chondrocytes (Fig. 4a). Further, to demonstrate whether mitochondrial transfer occurs in the cartilage in situ, we used Cag^{cre}PhAM^{floxed} mice (chondrocytes expressing mito-Dendra2). Dendra2 is a green/red photo-switchable protein whose green fluorescence can be irreversibly converted to red fluorescence upon exposure to a 405 nm laser. We exposed the cartilage of tibia plateau isolated from Cag^{cre}PhAM^{floxed} mice (chondrocytes expressing mtD2) to 405 nm laser, for switching the fluorescence of mitochondria from green to red in a designated area (Fig. 4b). The ex vivo mouse proximal tibia were cultured for 2 days to allow the transfer of mitochondria emitting red fluorescence to other chondrocytes with mitochondria emitting only green fluorescence in an area not activated by laser. We observed red fluorescent mitochondria in unexposed chondrocytes, suggesting in situ mitochondrial transfer between chondrocytes (Fig. 4b). Of note, by co-culturing chondrocytes which was transplanted with green-fluorescent osteocyte mitochondria (OY-mtD2-AC) with mT-AC and analyzed by FCM (Fig. 4c), we validated that osteocyte mitochondria can also be transferred between chondrocytes (Fig. 4c). Further, by transplanting mitochondria from mouse osteocyte cell line into the mT-AC and mtD2-AC co-culture system, we found that this osteocyte mitochondria within chondrocytes strongly enhanced mitochondrial transfer between chondrocytes (Fig. 4a), implicating the regulatory role of osteocyte mitochondria throughout the full thickness of cartilage. To study the association of chondrocyte mitochondrial transfer and inflammation, we mimicked inflammatory stimulation in OA via treating primary chondrocyte with IL-1β to generate OA-AC (Fig. 4d). We then transplanted mitochondria isolated from OA-AC into healthy chondrocytes, and found this mitochondrial transfer also activates the cGAS-STING pathway (Figs. 4e and S5k). The subsequent downstream expression of matrix-degrading enzymes and inflammatory cytokines were elevated in recipient chondrocytes in vitro as well, which could be blocked by STING inhibitor H-151 (Figs. 4e, f and S5l). Therefore, osteocyte mitochondria amplify inflammatory signals by enhancing mitochondrial transfer between chondrocytes.

We then examine whether osteocyte mitochondria amplify synovitis via chondrocytes. Synovial macrophages are recognized as the primary inflammatory cells during OA[36]. We isolated macrophage from mG/mT mice-cell membrane of macrophage was labeled with green fluorescence protein (mG-MΦ). By FCM analysis, we found

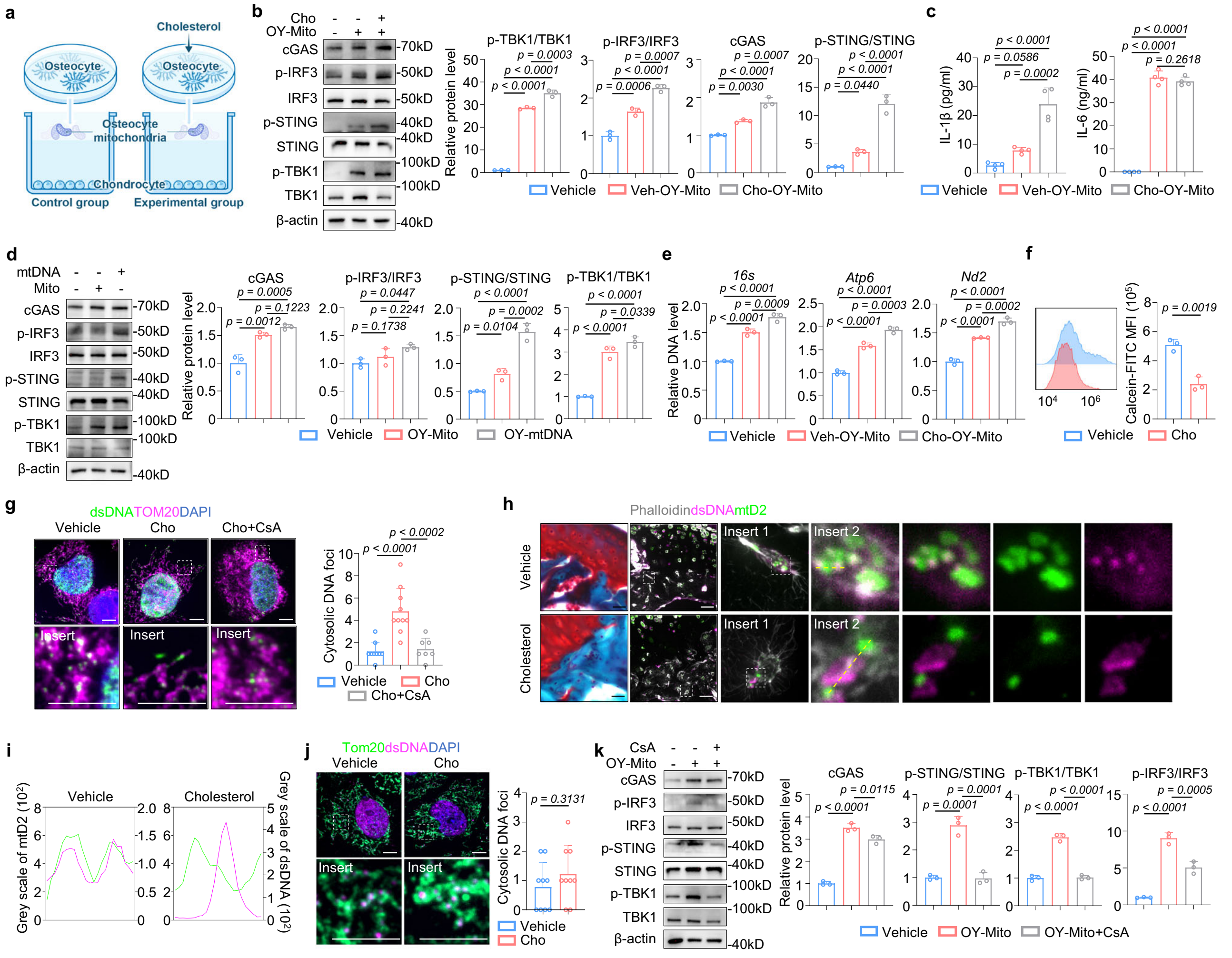

Fig. 5 | Cholesterol metabolism permeabilize osteocyte mitochondrial membrane to release mtDNA during OA. a Schematic and **b** western blot analysis and quantitative results of cGAS-STING pathway (n = 3 per group) and **c** cytokines in the supernatant (n = 4 per group) of chondrocytes receiving CHO-OY-Mito. **d** Western blot analysis of cGAS-STING pathway of chondrocyte transplanted with osteocyte mitochondria/mtDNA (n = 3 per group). **e** Cytosolic mtDNA gene level of chondrocyte transplanted with receiving CHO-OY-Mito (n = 3 per group). **f** FCM analysis of mPTP permeability of mouse osteocyte cell line treated with cholesterol (n = 3 per group). **g** Confocal image of mouse osteocyte cell line treated with cholesterol and cyclosporin A (CsA) (n = 9 for vehicle group, n = 10 for cholesterol group and n = 7 for CsA group). **h** Confocal image of joint tissue of Cag^{cre} PhAM^{floxed} mice cultured ex vivo for 2 days under 100 μM cholesterol and **i** fluorescence intensity analysis. Scale bar: 100 μm. **j** Confocal image of chondrocytes treated with cholesterol (n = 9 per group). **k** Western blot analysis of cGAS-STING pathway of chondrocyte transplanted with receiving CHO-OY-Mito that treated with CsA (n = 3 per group). Data are presented as the mean ± SD, with biologically individual data points shown. *p* values were determined using unpaired two-tailed Student's *t* test (**f**, **j**), and one-way ANOVA with post hoc Šídák test (**b**–**e**, **g**, **k**). Source data are provided as a Source data file.

chondrocytes transplanted with osteocyte mitochondria (OY-Mito-AC) significantly induced M1 polarization in co-cultured mG-MΦ when compared to vehicle chondrocytes (Veh-AC) (Fig. 4g), which may due to the secreted cytokines by chondrocytes (e.g., IL-6). In contrast, vehicle chondrocytes promoted M2 polarization of mG-MΦ, which was abolished when osteocyte mitochondria were transplanted into chondrocytes (Fig. 4h). To further study this, we cocultured macrophage with conditioned medium of chondrocytes transplanted with osteocyte mitochondria and found M1-related gene were upregulated (Fig. 4i) and-M2 related gene were downregulated (Fig. 4j), indicating that osteocyte mitochondria contribute to joint inflammation by modulating synovial macrophage through their transfer to chondrocytes.

Cholesterol permeabilizes osteocyte mitochondrial membrane to release mtDNA during OA

Increased cholesterol level in osteocyte impaired its mitochondrial function in OA (Fig. S3e). Therefore, we treated mouse osteocyte cell line with cholesterol and transplanted its mitochondria (Cho-OY-Mito) into primary chondrocytes (Fig. 5a). Notably, Cho-OY-Mito induced more severe cGAS-STING activation and the expression of proinflammatory cytokines in comparison with mitochondria from vehicle mouse osteocyte cell line (Veh-OY-Mito) (Fig. 5b, c). This led us to explore the underlying mechanism of cholesterol in regulating osteocyte mitochondria. cGAS-STING pathway senses cytosolic double-strand DNA[37], and mitochondria retain their own DNA (mtDNA)[38]. Consistently, compared to osteocyte mitochondria, their isolated mtDNA markedly induced cGAS-STING activation in chondrocytes (Fig. 5d). We found that Cho-OY-Mito induced higher cytosolic mtDNA stress in comparison with OY-Mito group (Fig. 5e). We then examined whether cholesterol regulates mtDNA release during OA. We observed that cholesterol significantly activated the osteocyte mitochondrial permeability transition pore (mPTP), which increased mitochondrial membrane permeability (Fig. 5f), and its mtDNA is prone to release into the cytosol (Fig. 5g). We then isolated joint tissue from Cag^{cre}PhAM^{floxed} mice and subjected to ex vivo culture under

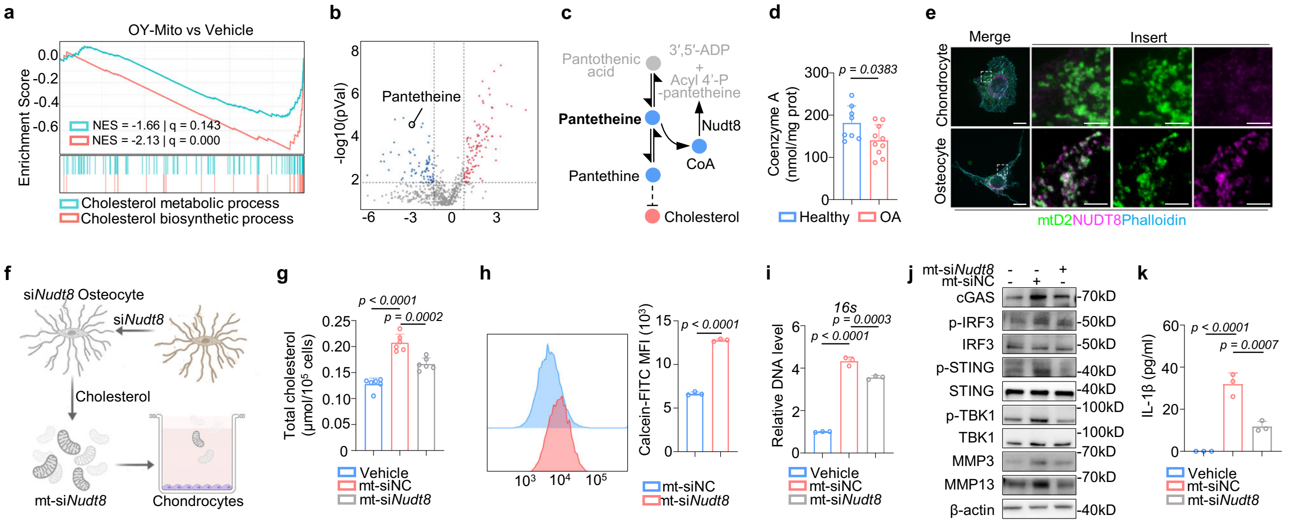

Fig. 6 | Nudt8 on osteocyte mitochondria regulates metabolic-inflammatory crosstalk in chondrocytes. a GSEA analysis showing de-enrichment of the cholesterol metabolic process and biosynthesis pathway of chondrocytes after osteocyte mitochondrial transplantation. **b** Volcano plot of the metabolomic results showing that pantetheine is significantly downregulated in chondrocytes receiving osteocyte mitochondria. **c** Schematic of metabolism of pantetheine. **d** Coenzyme A level in cartilage from OA patient (n = 8 for healthy control and n = 10 for OA group). **e** Immunofluorescence of Nudt8 expression in mtD2-AC and mtD2-OY. Scale bar: 10 μm; Insert scale bar: 2 μm. **f** Schematic of chondrocytes transplanted with mt-si*Nudt8*. **g** Total cholesterol levels (n = 6 per group), **h** FCM analysis of mPTP permeability (n = 3 per group), **i** cytosolic mtDNA gene level (n = 3 per group), **j** western blot analysis of cGAS-STING pathway and **k** cytokines in the supernatant (n = 3 per group) of chondrocytes receiving mt-siNC or mt-si*Nudt8*. Data are presented as the mean ± SD, with biologically individual data points shown. *p* values were determined using unpaired two-tailed Student's *t* test (**d**, **h**), and one-way ANOVA with post hoc Šídák test (**g**, **i**, **k**). Source data are provided as a Source data file.

100 μM cholesterol treatment. Confocal imaging and histological analysis revealed that subchondral osteocytes in the cholesterol-treated group exhibited mtDNA release from mitochondria to cytosol after two days of culture (Fig. 5h, i), consistent with previous in vitro findings. However, supplementation of cholesterol in vitro showed minimal effects on primary chondrocytes (Fig. 5j). Notably, inhibiting mPTP with cyclosporin A (CsA) effectively attenuated cholesterol-induced mtDNA release in mouse osteocyte cell line (Fig. 5g). Mitochondria isolated from CsA- and cholesterol-treated mouse osteocyte cell line showed less activation of the cGAS-STING pathway in chondrocytes in comparison with cholesterol-treated group (Fig. 5k). These findings demonstrate that cholesterol promotes mPTP formation in osteocyte mitochondria, leading to mtDNA release and triggering inflammation in chondrocytes.

Nudt8-enriched mitochondria in osteocytes governs metabolic-inflammatory crosstalk in chondrocytes

Our bulk RNA-seq analysis indicated that chondrocytes receiving osteocyte mitochondria exhibited a downregulation of cholesterol metabolism/biosynthetic pathway (Fig. 6a). Excessive cholesterol content in chondrocytes was observed (Fig. S6a, b), and dysregulated cholesterol metabolic genes (*Hmgcs1, Cyp51, Insig1* and *Angptl4*) were validated in chondrocytes receiving osteocyte mitochondria (Fig. S6c). Given that previous results demonstrated osteocyte mitochondria regulate inflammation, we further explored how osteocyte mitochondria coordinate the "metabolic-inflammatory" features in chondrocytes during OA pathogenesis. We first performed metabolomics analysis, which revealed that pantetheine, an important intermediate in cholesterol metabolism[39], was decreased in primary chondrocytes receiving osteocyte mitochondria (Fig. 6b). Pantetheine is the active form of pantothenic acid (PA) and typically exists as its corresponding disulfide form, pantethine. Pantethine is an intermediate in the production of Coenzyme A (CoA) and plays a significant role in lipid metabolism (Fig. 6c)[40]. We found that CoA levels were decreased in human OA cartilage (Fig. 6d). Recently, Nudt8 was identified as a CoA-degrading enzyme localized in mitochondria[41]. We observed that, although expressed in both cell types, mouse osteocyte cell line harbors a mitochondrial subpopulation enriched in Nudt8, but absent in primary chondrocytes (Figs. 6e and S6d). We found that cholesterol does not regulate the content of NUDT8 in osteocyte (Fig. S6e). To examine the role of osteocyte mitochondrial Nudt8 in regulating chondrocytes, we knocked down Nudt8 in mouse osteocyte cell line, which had little impact on mitochondrial mass (Fig. S6f, g), but downregulated Nudt8 content in osteocyte mitochondria (Fig. S6h). We then isolated their mitochondria (mt-si*Nudt8*) and transplanted them into chondrocytes (Fig. 6f). We found that transplanting either mt-siNC or mt-si*Nudt8* had minimal effect on *Nudt8* expression by chondrocyte (Fig. S6i), but in comparison with mitochondria from mouse osteocyte cell line transfected with nonsense siRNA (mt-siNC), mt-si*Nudt8* lost the ability to increase cholesterol levels in recipient chondrocytes (Fig. 6g). Additionally, primary chondrocyte transplanted with mt-si*Nudt8* showed lower mPTP permeability (Fig. 6h) and cytosolic mtDNA content in comparison with mt-siNC group (Figs. 6i and S6j). Consequently, mt-si*Nudt8* failed to activate the cGAS-STING pathway (Figs. 6j and S6k), downstream inflammation markers (*Isg15, Ifit1, Irf7, Cxcl10, Il6* and *Il1b*), supernatant cytokines (Figs. 6k and S6l, m), and matrix-degrading enzymes (*Mmp3* and *Mmp13*) in primary chondrocytes (Figs. 6j and S6k, 6n). These results indicate that Nudt8 in osteocyte mitochondria regulates metabolic-inflammatory crosstalk in chondrocytes.

Targeting metabolic-inflammatory crosstalk alleviates OA

To target the Nudt8-regulated metabolic-inflammatory crosstalk in chondrocytes, we evaluated the potential of pantethine in alleviating OA. Though did not downregulate *Nudt8* expression (Fig. S7a), pantethine treatment significantly improved cholesterol-impaired oxidative phosphorylation of mouse osteocyte cell line (Fig. S7b), and reduced cholesterol-induced mPTP activation (Fig. 7a), mtDNA release in osteocyte mitochondria (Fig. 7b). Further, cholesterol-induced mitochondrial transfer from mouse osteocyte cell line to primary chondrocytes was downregulated by pantethine (Fig. 7c). Osteocyte mitochondria induced cholesterol accumulation and increased

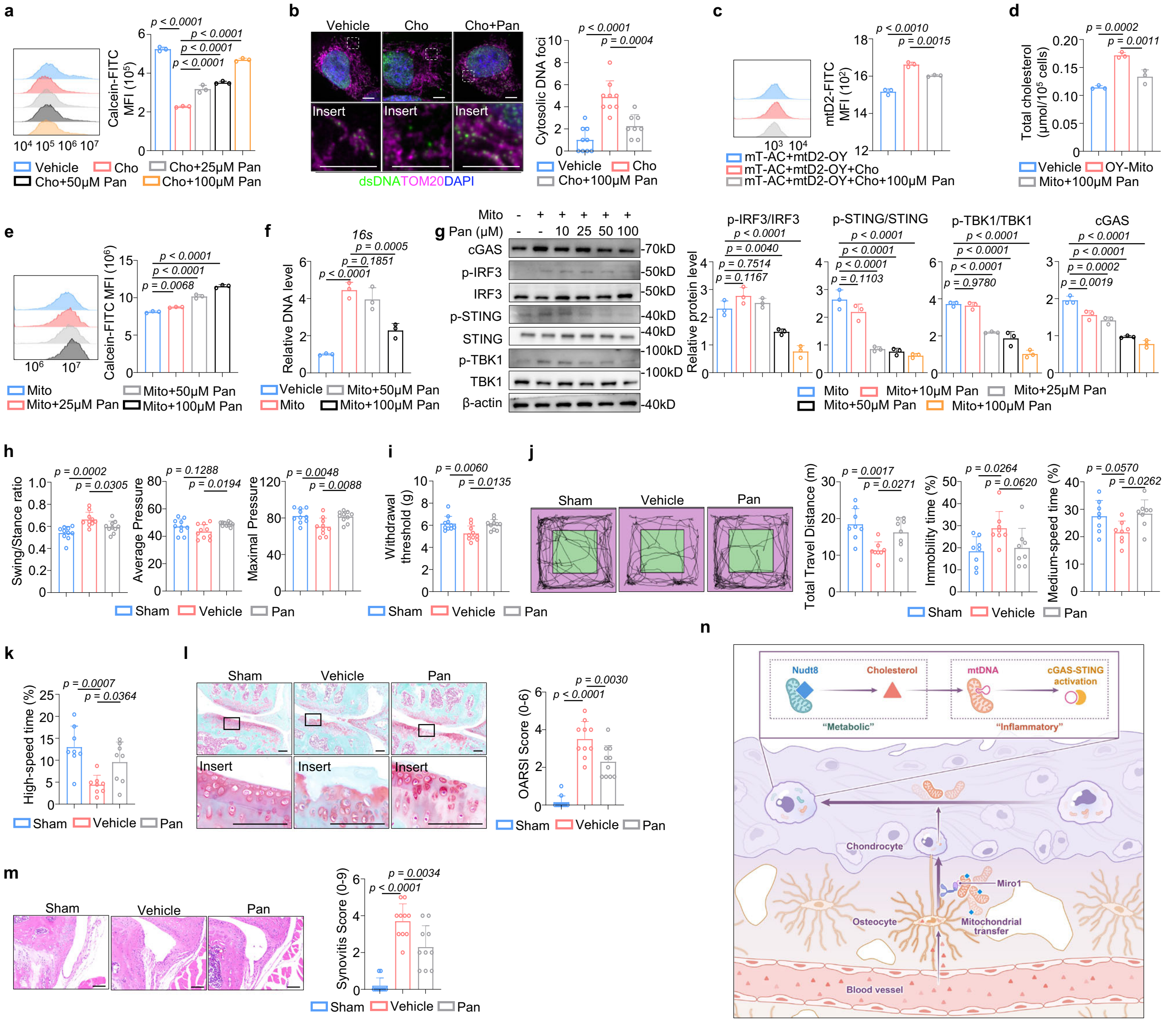

Fig. 7 | Targeting metabolic-inflammatory crosstalk alleviates OA. a FCM analysis of mPTP permeability of osteocytes under cholesterol and pantethine (Pan) treatment (n = 3 per group). **b** Immunofluorescence showed the colocalization of TOM20 and mtDNA in osteocytes under cholesterol and pantethine treatment (n = 9 for vehicle and cholesterol group and n = 8 for pantethine group). **c** FCM analysis of FITC-A intensity of mT-AC cocultured with mtD2-OY under cholesterol stimulation and pantethine treatment (n = 3 per group). **d** Total cholesterol levels, **e** FCM analysis of mPTP permeability, **f** cytosolic mtDNA gene level and **g** western blot analysis of cGAS-STING pathway in chondrocytes receiving osteocyte mitochondria treated with pantethine (n = 3 per group). **h** Gait pattern quantitative results (n = 10 per group), **i** von Frey tests (n = 10 per group), **j**, **k** open field tests (n = 8 per group), **l** a representative image of safranin-O staining and OARSI scores and **m** a representative image of H&E and synovitis scores (n = 10 per group) of DMM model of male mice with oral administration of pantethine. Scale bar: 100 μm. **n** Graphic abstract of the study. Data are presented as the mean ± SD, with biologically individual data points shown. *p* values were determined using one-way ANOVA with post hoc Šídák test. Source data are provided as a Source data file.

mitochondrial membrane permeability in primary chondrocytes (Figs. 7d and S7c), and pantethine restored cholesterol metabolism-related gene expression in a dose-dependent manner in primary chondrocytes receiving osteocyte mitochondria (Fig. S7d, e), and significantly reduced its excessive cholesterol accumulation (Figs. 7d and S7f) without regulating chondrocyte *Nudt8* expression (Fig. S7e). This led to decreased mitochondrial membrane permeability (Fig. 7e) and cytosolic mtDNA content in recipient chondrocytes (Figs. 7f and S7g), ultimately reducing the activation of the cGAS-STING pathway in chondrocytes (Figs. 7g and S7h). Moreover, pantethine treatment significantly reduced expression of pro-inflammatory genes (*Il1b* and *Il6*) and matrix-degrading genes (*Mmp3* and *Mmp13)* in primary chondrocytes that received osteocyte mitochondria (Fig. S7h). Pantethine also rescued impaired matrix synthesis in recipient chondrocytes (Fig. S7i). To verify the in vivo effects of pantethine, we first performed intra-articular injections in two PTOA models, including DMM and anterior cruciate ligament transaction (ACLT). Pain behavior was improved (Fig. S8a–d), and OA-related cartilage deterioration (Fig. S8e, f) and synovitis (Fig. S8g) were ameliorated in pantethine-treated mice. No significant sex difference was observed (Fig. S8h–n). We further performed a chemical-induced OA mouse model using intra-articular monosodium iodoacetate (MIA) injection and found pantethine improved pain behavior and ameliorated histological changes of OA mice as well, with no significant sex difference (Fig. S9).

Pantethine has been approved by the National Medical Products Administration, and oral administration of pantethine modulates low-density lipoprotein cholesterol metabolism, offering therapeutic benefits for cardiovascular and neurodegenerative diseases[42,43]. We considered oral delivery to be well-accepted by patients, prompting further assessment of its therapeutic effects in OA. The body weight of the pantethine-treated group was comparable to that of the vehicle group (Fig. S10a). Histological analysis of the heart, liver, kidney, and spleen revealed minimal toxicity associated with pantethine treatment (Fig. S10b). Blood routine tests showed that white blood cell (WBC) count, red blood cell (RBC) count, platelet (PLT) count, and other subcellular fractions were within normal ranges for the pantethine-treated group (Fig. S10c). Consistent with the results from intra-articular delivery, oral administration of pantethine also ameliorated OA progression. This was demonstrated by improved gait patterns (Figs. 7h and S10d), von Frey test (Fig. 7i), open field tests (Fig. 7j, k), and reduced cartilage deterioration, as evidenced by improved OARSI (Figs. 7l and S10e), and synovitis scores (Fig. 7m) compared to vehicle treatment in OA models. Further, pantethine treatment showed no apparent sex difference in body weight (Fig. S10f), histological analysis of organs (Fig. S10g) and blood routine tests (Fig. S10h). The treatment effect of pantethine on pain behavior tests (Fig. S10i–m), cartilage deterioration and synovitis scores in female OA models were also validated (Fig. S10n–p). These data further support the conclusion that targeting the metabolic-inflammatory crosstalk in osteocyte mitochondria via pantethine supplementation efficiently ameliorates OA progression in vivo (Fig. 7n).

Discussion

As lifestyle factors continue to affect populations worldwide, the incidence of metabolic disorders, such as hypercholesterolemia and its associated OA is on the rise[44]. In this study, we focused on the metabolic-inflammatory crosstalk in OA and found that disrupted cholesterol metabolism exacerbates cartilage inflammation and joint deterioration. Mechanistically, osteocyte mitochondria act as signal shuttles, targeted by cholesterol for intercellular transfer to chondrocytes. Disrupted cholesterol metabolism regulates the permeability of osteocyte mitochondria, leading to the release of mtDNA and activation of the cGAS-STING pathway in chondrocytes, which lead to joint inflammatory microenvironment and synovitis in OA. Specifically, Nudt8 in osteocyte mitochondria acts as a metabolic-inflammatory switch, accelerating OA progression and revealing itself as a potential target for OA treatment.

Cartilage is avascular[45], leading the mechanism of how metabolic or inflammatory signals were triggered remains elusive. Emerging studies revealed that mitochondria could transfer intercellularly in various route independently of blood vessels[31], suggesting a potential route for tissue communication. In diarthrodial joint, osteochondral units composed of articular cartilage and subchondral bone with calcified cartilage tightly anchoring it together, have the unique capability of transferring loads during weight-bearing and joint motion with abundant intercellular crosstalk within it[28]. Among the diverse cell types in subchondral bone, osteocytes are not only the most abundant but also serve as critical regulators of skeletal homeostasis. Notably, osteocytes are the only cells that, to our knowledge, establish direct physical connections with chondrocytes through specialized intercellular nanotubes. These osteocyte-chondrocyte nanotubes represent the observed inter-tissue cellular nanotubular structures in vivo, uniquely bridging bone and cartilage compartments, led the osteocyte may as the intermediaries of systemic factors influencing cartilage. Morphologically, osteocytes and blood vessels in cortical bone are in close proximity[46], and our previous study demonstrated direct physical contact between osteocytes and endothelial cells[29]. Cholesterol uptake from the blood has key roles in maintaining cellular cholesterol homeostasis, as it is a water-insoluble molecule that must be packaged by lipoproteins for transport within the plasma[47]. The anatomical proximity of osteocyte and blood vessels may facilitate cholesterol uptake, suggesting that osteocytes serve as important cholesterol-responsive cells[48]. Our study revealed the structure of the EOC, identifiable in both weight-bearing and non-weight-bearing regions of the osteochondral unit, with no significant dendritic morphological changes observed during OA. This structure appears to transduce metabolic-inflammation signals during OA progression. However, several methods have been used for the regulation of intercellular nanotubes formation (e.g., Cytochalasin B[33], si-*Tnfaip2*[49]), yet currently there are no well-established methods to precisely target nanotube formation in vivo, and further mechanistic validation is needed.

To address the synergistic metabolic-inflammatory changes in OA, we focused on the dual role of mitochondria. From an evolutionary perspective, the endosymbiotic theory proposes that mitochondria originated from an ancient symbiotic relationship between a primitive eukaryotic cell and an ancestral aerobic bacterium. Over time, the engulfed bacteria lost much of their independent functionality, ultimately evolving into mitochondria[50]. This symbiotic relationship provided the host cell with a more efficient energy production system[51]. The cGAS-STING pathway plays a critical role in monitoring and maintaining this endosymbiosis, helping the cell recognize potential threats and preventing harmful microbial invasion[37]. However, mitochondria retain their own DNA, which can leak into the cytoplasm under cellular stress or damage. This can overstimulate the cGAS-STING pathway, leading to chronic inflammation and cellular damage[52]. The dual role of mitochondria makes them strong candidates for mediating the regulation of chondrocytes by osteocytes. Our group demonstrated that as a vital signaling cells, osteocytes regulated various biological process, such as angiogenesis, tumor suppression, and osteoblast-osteoclast balance via intercellular mitochondrial transfer[22,29,53]. In contrast to other cell types, chondrocytes reside in avascular and hypoxia environment[54], which gives them a unique metabolic state and mitochondrial homeostasis[55]. Mitochondrial dysfunction has long been considered as features of OA cartilage[56]. We found that osteocyte mitochondrial transfer to chondrocytes was enhanced during OA progression. Surprisingly, osteocyte mitochondria not only failed to rescue chondrocytes but transmit inflammatory signals intercellularly by directly increasing cytosolic DNA stress and triggering mitochondrial transfer. Further, our study revealed increased mitochondrial membrane permeability in recipient chondrocytes. Though this need further validation due to technical limitation, it may due to the mPTP activation of endogenous chondrocyte mitochondria, which may serve as a mechanism transmitting inflammatory signals within chondrocytes. These exacerbated OA phenotype of chondrocytes, further regulating synovial macrophage polarization, likely due to cytokine secretion (e.g., IL-6) by chondrocytes. This suggests that osteocyte mitochondria are not merely metabolic organelles but also complex signaling shuttles that regulate inflammation and various cellular functions involved in OA. These findings provide a new perspective on the triggering of inflammation in avascular tissues, suggesting that inflammatory signals may be amplified through intermediate cells and intercellular mitochondrial transfer. Besides, osteocytes are established as endocrine cells capable of secreting diverse cytokines, the crosstalk between mitochondria and other osteocyte-derived signals may provide a more comprehensive mechanistic framework, and this inflammatory triggering mechanism warrants further investigation to better understand the pathogenesis and treatment of inflammatory diseases.

In fact, the pathogenesis of OA and many other diseases, such as cardiovascular and neurodegenerative diseases, is closely related to inflammation and metabolism, in which mitochondria play an important role[57]. Due to the dual regulatory role of mitochondria, understanding the mechanisms that regulate “metabolic-inflammatory” shift of mitochondria and its impact on disease progression is of great importance. To address this, we demonstrated that osteocyte mitochondria disrupt cholesterol metabolism in chondrocytes, with excessive cholesterol inducing osteocyte mitochondrial mPTP activation and mtDNA leakage, which shifts them toward an inflammatory phenotype. To further address the underlying mechanism, we identified pantetheine, an intermediate in the production of coenzyme A and closely related to cholesterol metabolism[42,43], as being significantly decreased by osteocyte mitochondria. This depletion occurs because mitochondria directly degrade CoA, leading to pantetheine depletion. We also identified Nudt8, which is expressed in osteocyte mitochondria and degrades CoA, further regulating cholesterol homeostasis. The expression of Nudt8 drives osteocyte mitochondria toward an inflammatory phenotype during intercellular transfer. These characteristics of Nudt8 suggest it as a potential regulator of the "metabolic-inflammatory" balance in osteocyte mitochondria. However, we currently lack tools to specifically track mitochondrial-Nudt8-dependent regulation within chondrocytes in vivo. Further studies are required to validate Nudt8 as the phenotypic switch point of osteocyte mitochondria in vivo. Additionally, exploring other potential switch targets within mitochondria warrants further investigation.

By targeting mitochondrial Nudt8 and its related metabolism, we treated chondrocytes with pantethine. Pantethine has been used for the treatment of hyperlipidemia, cardiovascular prevention, and in children with pantothenate kinase-associated neurodegeneration[42,58]. We performed oral treatment in different OA models and showed promising results. As it is one of the metabolites present in the human body, the safety and efficacy is reliable, though the delivery strategy of pantethine requires further study.

Our study has limitations. Recent studies have indeed shown mitochondria exist as functionally distinct subpopulations within cells[59,60]. The physiological intercellular transfer of mitochondrial subpopulations may involve complex selection mechanisms, and their biological functions cannot be fully captured in our mitochondrial transplantation system. Future work will focus on characterizing mitochondrial subpopulations and elucidating their functional roles in this transfer mechanism. Besides, PTOA and CIOA models may not fully replicate the slow progression of aged or spontaneous OA, and our findings may require further validation in such models. While the major results of our work is successfully demonstrated the critical biological phenomenon of cholesterol-regulated intercellular mitochondrial transfer and its significant role in OA, it does not directly address the fundamental underlying mechanisms driving cholesterol-associated OA pathogenesis, as short-term HCD mice model does not reflect the cholesterol intake of middle aged and older individuals, which may not fully capture the distinct pathological responses in cholesterol-associated OA, therefore might hinder the clinical translation. Future studies employing long-term cholesterol treatment in aging models and $Dmp1^{cre}PhAM^{floxed}$ OA model will help bridge this gap and further elucidate the role of mitochondrial-related metabolic dysregulation in OA progression.

In conclusion, our study provides a novel target for metabolic diseases closely associated with inflammation. Mitochondria in different tissues have unique functional proteins that regulate various metabolic process[61]. Targeting the mitochondrial phenotype may be a potential approach for treating these diseases, and pantethine has potential as a therapeutic agent for OA treatment.

Methods

Mouse model

All experiments were carried out under the guidelines of the Institutional Animal Care and Use Committee (IACUC) at Shanghai Jiao Tong University, affiliated Shanghai Sixth People's Hospital and were performed with IACUC-approved protocols (No. DWLL2023-0594). Wild-type male and female C57BL/6 J mice were purchased from Vital River Laboratory. mT/mG, $Miro1^{floxed}$ and $PhAM^{floxed}$ were from Jackson laboratory. Cag^{Cre}, $cGAS^{floxed}$, and mG/mT mouse strains were purchased from GemPharmtech. The 9.6-kb $Dmp1^{cre}$ transgenic mice were provided by J. Q. (Jerry) Feng at Texas A&M College of Dentistry, USA. $Col2a1^{creERT2}$ transgenic mice were provided by Professor Liu Yang at Xijing Hospital, Fourth Military Medical University, China. For activation of creERT2 in adult mice, 150 mg/kg body weight of tamoxifen in corn oil was injected intraperitoneally into 4-week-old mice once a day for 5 consecutive days. Littermate controls were used for all experiments. All mice had ad libitum access to food and water and were maintained in an SPF facility with a 12 h:12 h light: dark cycle, a temperature of 22 ± 2 °C, and humidity of 50 ± 10%. All cages were supplied with nesting materials and environmental enrichment devices. Animals were monitored daily by trained research staff for general health, behavior, and any signs of distress.

For OA model establishment, 10-week-old mice were randomly assigned to each treatment group and surgery was performed under isoflavone inhaling anesthesia. To establish the surgically induced DMM PTOA model, the medial meniscotibial ligament in the left knee was sectioned with a blade to destabilize the medial meniscus. To establish the surgically induced ACLT PTOA model, the anterior cruciate ligament in the right knee was sectioned with a blade. To establish chemically induced MIA OA model, 0.1 mg of MIA in 6 μl of 0.9% sterile saline was intra-articularly injected in the right knee. H-151 (Topscience, T5674) was intra-articular injected at 5 ng 2 times a week. Pantethine (MedChemExpress, HY-B1028) was intra-articular injected at 500 ng 2 times a week or orally delivered at 150 mg/kg per day by dissolved in water[62]. Mice were analyzed 8 weeks after DMM surgery, 4 weeks after ACLT surgery or MIA injection, respectively. Mice were euthanized for tissue harvesting by carbon dioxide asphyxiation.

Mice were fed with maintenance diet (Jiangsu Xietong Pharmaceutical Bio-engineering Co., Ltd, 1010009) as regular diet. HCD mice generation and DMM model duration were based on prior literature[11]. In brief, 5-week-old male and female mice were fed with maintenance diet supplemented with 2% cholesterol. DMM surgery was performed after seven weeks of RD or HCD and analyzed 5 weeks after DMM surgery.

Human subjects

All experiments were approved by the Ethics Committee of Shanghai Sixth People's Hospital (NO. 2023-KY-024(K)). Cartilage samples of patients were collected from the Department of Orthopedics, Shanghai Sixth People's Hospital, affiliated to Shanghai Jiao Tong University School of Medicine between March 2023 and September 2023. A total of 10 hip OA cases and 8 femoral head fracture cases were finally recruited, and written informed consent was obtained from all participants for the use of their sample for research purposes before the operative procedure. Patients underwent total hip replacement, and the cartilage species were collected for further study.

Behavior tests

Gait parameters of freely moving mice were measured by a computerized video-based CatWalk gait analysis system. Each mouse experienced three trials. Briefly, a mouse was placed on an elevated glass platform located in a dark room and was allowed to move freely. A light beam below the platform illuminated the surface, which made an image of every footprint and was recorded by a camera. The Visugate software (Shanghai XinRuan Technology) calculated gait parameters for statistical analysis.

Von Frey test was applied with increasing force intensities on the plantar surface of the hindpaw of the mouse, which is placed in an elevated grid floor chamber to determine the tactile pain threshold using an electronic Von Frey instrument (Bioseb). Ten trials were subjected to hind paws with a 30-s interval maintained between trials.

For open field test, mice were placed individually in a square clear chamber (40 × 40 cm) and allowed to freely explore for 5 min under normal lighting, with movement and trajectories videoed and analyzed by a computerized system.

Isolation and expansion of mice chondrocytes

Articular chondrocytes were isolated from cartilaginous portions of the femoral heads, femoral condyles, and tibial plateau. Cartilage tissue was finely minced and digested with 0.1% collagenase type II in DMEM at 37 °C for 60 min, followed by 0.05% collagenase type II at 37 °C overnight. A single-cell suspension was passed through a 70 μm cell strainer, centrifuged at 400 g for 4 min and resuspended in DMEM supplemented with 10% Fetal bovine serum and 1% Penicillin-Streptomycin. The isolated cells were cultured at 37 °C in 5% CO_2. Articular chondrocytes cultured for no more than passage 1 were used in subsequent experiments.

Generation of mtD2-OY

Mito-Dendra2 (mtD2) was amplified from a plasmid (https://www.addgene.org/55796/) and cloned into the modified pHAGE vector containing Flag using the restriction enzymes *NotI* and *BamHI*. Then, the full-length mtD2 open reading frame was removed from the plasmid and inserted into the pHAGE vector, and the DNA sequence was confirmed. Lentivirus were produced by co-transfection of the plasmids with VSVG and Δ8.9 plasmids into HEK293T cells following the protocol provided by Open Biosystems (GE Healthcare, United States). MLO-Y4 cell line was obtained from Cyagen Biosciences (Cat: M7-0401). MLO-Y4 cells were cultured for 2 days, infected with lentivirus for 24 h, and treated with puromycin for 48 h.

Generation of Miro1-KD mtD2-OY

The shRNA oligonucleotides were synthesized by Tsingke Biotechnology Co., Ltd. (Beijing, China), and the sequences were 5′-GCTCAACTTCTTCCAGAGAAT-3′ and 5′-GATATCTCAGAGTCGGAA TTT-3′. The double oligonucleotides were cloned into the pLKO.1-hygro lentivirus vector. HEK-293T cells at 70% confluency were co-transfected with shRNA and the lentivirus packaging plasmids, psPAX2 and pMD2.G. The lentiviral particles were harvested from the medium after 48 h of co-transfection. mtD2-OY were transduced with lentivirus for 48 h, and stable cell lines were selected using 500 μg/mL hygromycin.

siRNA transfection

The siRNA sequences for the target gene markers were synthesized by Genomeditech. Cells were seeded in a six-well plate or 15-cm dish. When 30% confluence was reached, cells were transfected with siRNA (50 nM) and Lipofectamine 3000 in Opti-MEM following the manufacturer's instructions. After a 4-h incubation, the medium was subsequently changed to a complete medium for another 48 h. The following were the siRNA sequences:

Nudt8 siRNA-1 forward: UCCCGACGACCAAGAUGUAAUtt
Nudt8 siRNA-1 reverse: AUUACAUCUUGGUCGUCGGGAtt
Nudt8 siRNA-2 forward: GAGGAGGUGGAUGAAGUAUUUtt
Nudt8 siRNA-2 reverse: AAAUACUUCAUCCACCUCCUCtt
Nudt8 siRNA-3 forward: CGUUGCUCUACACGCUGCGUUtt
Nudt8 siRNA-3 reverse: AACGCAGCGUGUAGAGCAACGtt
Cgas siRNA-1 forward: GGAUUGAGCUACAAGAAUAtt
Cgas siRNA-1 reverse: UAUUCUUGUAGCUCAAUCCtt
Cgas siRNA-2 forward: GGACAAAUUGAGAUUGAAAtt
Cgas siRNA-2 reverse: UUUCAAUCUCAAUUUGUCCtt
Cgas siRNA-3 forward: GAAUUUGAUGUUAUGUUUAtt
Cgas siRNA-3 reverse: UAAACAUAACAUCAAAUUCtt
Sting1 siRNA-1 forward: GGAUUUUAUAUAUGUAGAAtt
Sting1 siRNA-1 reverse: UUCUACAUAUAUAAAAUCCtt
Sting1 siRNA-2 forward: GCAUCAAGAAUCGGGUUUAUUtt
Sting1 siRNA-2 reverse: AAUAAACCCGAUUCUUGAUGCtt
Sting1 siRNA-3 forward: CAACUGCCUUCUUAAUAAAtt
Sting1 siRNA-3 reverse: UUUAUUAAGAAGGCAGUUGtt

Mitochondria isolation

To isolate enough mitochondria, cells were cultured in 15 cm culture dishes. The cells were collected upon reaching 90% confluence. Mitochondria were isolated using a mitochondria isolation kit for mammalian cells (ThermoFisher, 89874). Briefly, cell pellets containing 2×10^7 cells were suspended into 800 μl of lysis buffer, incubated on ice for 5 min with vortexing at maximum speed every minute, followed by centrifugation at 700 g for 10 min at 4 °C. The supernatant was centrifuged at 12,000 × *g* for 15 min at 4 °C. The mitochondrial pellets were rinsed and centrifuged at 12,000 × *g* for 5 min at 4 °C. The isolated mitochondria were applied freshly for subsequent characterization.

Subcellular fractionation

In brief, cells were harvested and lysed in digitonin lysis buffer (150 mM NaCl, 50 mM HEPES pH 7.4, 25 μg/ml digitonin, protease, and phosphatase inhibitors) on ice for 10 min, followed by centrifuged for 10 min at 16,000 × *g* at 4 °C, and the supernatant was the clean cytosolic fraction that split into two fractions for DNA extraction and western blotting. The initial pellet from the first centrifugation was lysed via NP-40 lysis buffer (150 mM NaCl, 50 mM HEPES pH 7.4, 1% NP-40, protease, and phosphatase 524 inhibitors) on ice for 30 min, followed by centrifuged at 16,000 × *g* for 10 min at 4 °C. The supernatant was the mitochondrial fraction stored for Western blotting analysis. The pellet fraction, which contains nuclei, was then lysed in RIPA buffer and split again for DNA extraction and protein detection.

DNA extraction and mtDNA copy number analysis

Total DNA was extracted using the FastPure Cell/Tissue Total RNA Isolation Kit (Vazyme, RC112-01) following the manufacturer's instructions. mtDNA and nuclear DNA contents were determined by amplifying a short region of the mitochondrially encoded *16S rRNA*, *Nd2*, *Atp6* and *18S rRNA* via quantitative RT-PCR, and the mtDNA copy number was calculated as the mtDNA/nDNA ratio.

Cholesterol assay

Cellular total cholesterol levels were measured using the Total Cholesterol Content Assay Kit (Solarbio, BC1985). In brief, cells were collected and lysed via ultrasound in ice bath. The levels of total cholesterol were determined according to the manufacturer's instructions. Serum cholesterol level was measured using Low-Density Lipoprotein Cholesterol (LDL-C) Content Assay kit (Solarbio, BC5335). Serum was collected and determined according to the manufacturer's instructions. For cholesterol staining of tissue, human osteochondral sample and mice joint were fixed in 4% PFA, decalcified in 10% EDTA and frozen sectioned in 10-μm slices. Sections were incubated with filipin complex (50 μg/mL, MedChemExpress, HY-N6716) 30 min in room temperature, mounted with ProLong Diamond antifade medium (ThermoFisher, P36961).

Seahorse analysis

The cell mitochondria respiration was assessed using the Seahorse Bioscience XF24 Analyzer. Cells were seeded at a density of 4×10^4 cells/well. Seahorse measurements were performed in FCS- and bicarbonate-free DMEM (pH 7.4) supplemented with 10 mM glucose, 2 mM glutamine, and 1 mM pyruvate. The mitochondria respiration of cell was evaluated using the Agilent Seahorse XF Cell Mito Stress Test, with sequential addition of 1.5 mM oligomycin, an inhibitor of ATP synthase, 1 mM carbonyl cyanide 4-(trifluoromethoxy) phenylhydrazone (FCCP), an uncoupling agent, and 0.5 mM rotenone and antimycin A (Rot/AA) to inhibit complex I and complex III of the respiratory chain, respectively. Data were analyzed using Wave (v2.6.3.5).

Western blotting

Tissue samples were homogenized and extracted by RIPA supplemented with a protease and phosphatase inhibitor cocktail (ThermoFisher, 78443). Cell samples and cell subfraction samples were extracted by RIPA supplemented with a protease and phosphatase inhibitor cocktail (ThermoFisher, 78443). Protein quantification was measured using a BCA assay kit. Protein bands were detected by conventional protocols for Western blotting. The following antibodies were used: Rabbit anti-VDAC (1:1000, Cell Signaling Technology, 4661), Rabbit anti-TOM20 (1:1000, Cell Signaling Technology, 42406), Rabbit anti-LAMIN A/C (1:1000, Cell Signaling Technology, 2032), Rabbit anti-MMP13 (1:1000, Abcam, ab39012), Rabbit anti-MMP3 (1:1000, Affinity, AF0217), Rabbit anti-ADAMTS5 (1:1000, Affinity, DF13268), Rabbit anti-STING (1:1000, Cell Signaling Technology, 50494), Rabbit anti-p-STING (1:1000, Cell Signaling Technology, 72971), Rabbit anti-cGAS (1:1000, Cell Signaling Technology, 31659), Rabbit anti-TBK1 (1:1000, Cell Signaling Technology, 3504), Rabbit anti-p-TBK1 (1:1000, Cell Signaling Technology, 5483), Rabbit anti-IRF3 (1:1000, Cell Signaling Technology, 4302), Rabbit anti-p-IRF3 (1:1000, Cell Signaling Technology, 29047), Rabbit anti-β-actin (1:3000, Affinity, AF7018), Rabbit anti-p-IKKα/β (1:1000, Cell Signaling Technology, 2697), Rabbit anti-p-p65 (1:1000, Cell Signaling Technology, 3033), Rabbit anti-p- IκBα (1:1000, Cell Signaling Technology, 2859), Rabbit anti-IKKα/β (1:1000, Affinity, AF6014), Rabbit anti-p65 (1:1000, Cell Signaling Technology, 8242), Rabbit anti-IκBα (1:1000, Affinity, AF5002), Rabbit anti-GAPDH (1:3000, Affinity, AF7021) and goat anti-rabbit IgG (H + L) HRP (1:3000, Cell Signaling Technology, 7074).

Mitochondria transplantation and mtDNA transfection

Recipient chondrocytes were seeded into 6-well plates. When cells reached 80% confluence, freshly isolated mitochondria at the indicated concentrations were seeded on top of the chondrocytes and co-incubate 3 h for western blot analysis of cGAS-STING pathway and 12 h for mRNA analysis. Mitochondria-transferred chondrocytes were used for subsequent experiments without further expansion. For mtDNA transfection, mtDNA was isolated from freshly isolated mitochondria using FastPure Cell/Tissue Total RNA Isolation Kit (Vazyme, RC112-01). Chondrocytes were transfected with mtDNA using Lipofectamine 3000 (ThermoFisher, 31985070) according to the manufacturer's instructions.

Flow cytometry

Cells digested from plates were washed in PBS and resuspended in FACS buffer. Flow cytometry was performed on a CytoFLEX Flow Cytometer. Flow cytometric results were analyzed with CytExpert (v2.3) and Flowjo (v10.8.1) software. Cells were gated on singlets and live cells.

ELISA and coenzyme A assay

The level of IL-1β and IL-6 of supernatant of chondrocytes were measured by ELISA according to the manufacture's instruction (Jonln Bio, JL18442, JL20268). For Coenzyme A assay, cartilage sample were homogenized and measured by a Coenzyme A Assay Kit according to the manufacture's instruction (Abnova, KA1664). Data were analyzed using SkanIt RE (v7.0.2).

RNA sequencing and analysis

Total RNA was isolated and purified using TRIzol reagent (ThermoFisher, 15596018) according to the protocol provided by the manufacturer. The quantity and purity of the RNA was determined using a NanoDrop ND-1000 (NanoDrop, Wilmington, DE, USA) and a Bioanalyzer 2100 (Agilent, CA, USA), respectively (concentrations > 50 ng/μL, RIN value > 7.0, total RNA > 1 μg). Next, mRNA with PolyA (polyA) was specifically captured by two rounds of purification using oligo (dT) magnetic beads (Dynabeads Oligo(dT), cat. 25-61005, Thermo Fisher, USA). The captured mRNA was fragmented using a magnesium ion fragmentation kit (NEBNextR Magnesium RNA Fragmentation Module, cat. E6150S, USA) at 94 °C for 5–7 min. The fragmented RNA was converted into cDNA by reverse transcriptase (Invitrogen SuperScript^{TM} II Reverse Transcriptase, cat. 1896649, CA, USA). Using E. coli DNA polymerase I (NEB, cat.m0209, USA) and RNase H (NEB, cat.m0297, USA), these complex duplexes of DNA and RNA were converted into DNA duplexes. A dUTP Solution (ThermoFisher, cat. R0133, CA, USA) was incorporated into the double-stranded DNA at the same time to blunt the ends of the double-stranded DNA. Then, an A base was added to each of the two ends, so that it could be connected with a linker containing a T base at the end, and the fragment size was screened and purified by magnetic beads. The second strand was digested with UDG enzyme (NEB, cat. m0280, MA, US), pre-denatured at 95 °C for 3 min by PCR, and denatured at 98 °C for a total of 8 cycles of 15 s each, annealed at 60 °C for 15 s, extended at 72 °C for 30 s, and finally extended at 72 °C for 5 min to generate a library (strand-specific library) with a fragment size of 300 ± 50 bp. Finally, we performed paired-end sequencing using an Illμmina Novaseq^{TM} 6000 (LC Bio-Technology CO., Ltd. Hangzhou, China) in PE150 sequencing mode following standard procedures.

Metabolomics

Total of 14 cell samples (n = 5 for vehicle group, n = 6 for OY-Mito group and n = 3 for pooled samples) were resuspended with prechilled 80% methanol. Then, the samples were melted on ice and centrifuged for 30 s. After sonification for 6 min, they were centrifuged and the supernatant was freeze-dried and dissolved in 10% methanol. Finally, the solution was injected into an LC-MS/MS system, and UHPLC-MS/MS analyses were performed using a Vanquish UHPLC system (ThermoFisher, Germany) coupled with an Orbitrap Q Exactive^{TM} HF-X mass spectrometer (ThermoFisher, Germany) in LCSW (Hangzhou, China). Samples were injected into a Hypesil Gold column (100 × 2.1 mm, 1.9 μm) at a flow rate of 0.2 mL/min. The eluents for the positive polarity mode were eluent A (0.1% FA in water) and eluent B (methanol). The eluents for the negative polarity mode included eluent A (5 mM ammonium acetate, pH 9.0) and eluent B (methanol). A Q Exactive^{TM} HF-X mass spectrometer was operated in positive/negative polarity mode with a spray voltage of 3.5 kV, capillary temperature of 320 °C, sheath gas flow rate of 35 psi, an auxiliary gas flow rate of 10 L/min, S-lens RF level of 60, and an auxiliary gas heater temperature of 350 °C.

The raw data files generated by UHPLC-MS/MS were processed using Compound Discoverer 3.1 (CD3.1, Thermo Fisher) to perform peak alignment, peak picking, and quantitation for each metabolite. The parameters were set as follows: retention time tolerance, 0.2 min; actual mass tolerance, 5 ppm; signal intensity tolerance, 30%; signal/noise ratio, 3; and minimum intensity. Next, the peak intensities were normalized to the total spectral intensity. The normalized data were used to predict the molecular formula based on additive ions, molecular ion peaks, and fragment ions. The peaks were matched with the mzCloud (https://www.mzcloud.org/), mzVault and MassList databases to obtain accurate qualitative and relative quantitative results. Statistical analyses were performed using the statistical software R (R version R 3.4.3), Python (Python 2.7.6 version), and CentOS (CentOS release 6.6).

The metabolites were annotated using the KEGG database (https://www.genome.jp/kegg/pathway.html), HMDB database (https://hmdb.ca/ metabolites), and LIPIDMaps database (http://www.lipidmaps.org/). The metabolites with VIP of >1, $P < 0.05$, and fold change of ≥2 or FC ≤ 0.5, were considered differential metabolites.

Quantitative RT-PCR

Total RNA was extracted using the EZ-press RNA Purification Kit PLUS (Ezbioscience, B0004DP). Complementary DNA was synthesized using

4× EZscript reverse transcription mix II (Ezbioscience, A0010GQ). PCR was performed in a volume of 10 μl. Complementary DNA (0.2 μl) was added to 2× Color SYBR green qPCR Master Mix (Ezbioscience, A0001-R1). All reagents used for RT-PCR were purchased from EZBioscience. PCR reactions were done using the QuantStudio™ 7 Flex real-time PCR System (v1.3).

Histology and immunofluorescence

Human cartilage and mouse knee joints were fixed in 4% PFA for 24 h, decalcified in 10% EDTA for 1 week. For Safranin-O or haematoxylin and eosin (H&E) staining, tissues were dehydrated and paraffin embedded, sectioned at a thickness of 5 μm. For immunohistochemistry and immunofluorescence, tissues were dehydrated in 30% sucrose for 4 h, embedded in OCT compound (Tissue-Tek), cut into 10 μm slices, and mounted onto adhesive slides. Sections were washed in PBS, permeabilized in 0.1% Triton X-100 in PBS for 5 min at room temperature, and incubated with 3% BSA-PBS for 30 min at room temperature to block nonspecific antibody binding. For immunofluorescence, the sections were incubated with antibody against Rabbit anti- collagen II antibody (1:100, Affinity, AF0135), Mouse anti-DNA antibody (1:200, Sigma-Aldrich, CBL186), Goat anti-CD31 antibody (1:200, R&D systems, AF3628) or Rabbit anti-NUDT8 antibody (1:100, Proteintech, 16098-1-AP), incubated with donkey anti-rabbit Alexa Fluor 488 secondary antibody (1:1000, Invitrogen, A-21206), goat anti-rabbit Alexa Fluor 568 secondary antibody (1:1000, Invitrogen, A-11011), Donkey anti-goat Alexa Fluor 568 secondary antibody (1:1000, ThermoFisher, A-11057), Alexa Fluor 647 phalloidin (1:250, Invitrogen, A22287), incubated with DAPI for 15 min, and mounted with ProLong Diamond antifade medium. Digital images were acquired using Olympus SpinSR and analyzed using Image J (Version 1.53c).

Statistics and reproducibility

Data are expressed as the mean ± standard deviation. Microscopy images shown are representative of at least 3 independent experiments. Detailed data processing, sample size and statistical methods for each result were shown in the corresponding figure legends. Statistical normality was made using the Shapiro-Wilk test. Statistical significance for normally distributed data was determined using a two-tailed Student's *t* test for comparisons of two groups. ANOVA with post hoc Šídák test was used when comparing multiple groups. Exact value of n can be found in the figures and legends. Statistical significance was set at $p < 0.05$. Statistical analysis was performed on GraphPad Prism (Version 9.1.1). All experiments described in this study were performed on independent samples.

Reporting summary

Further information on research design is available in the Nature Portfolio Reporting Summary linked to this article.

Data availability

All the data and code needed to understand and assess the conclusion of this research are available in the main text, Supplementary Materials, GEO database (accession numbers GSE220168 for RNA-seq and GSE104782 for published single-cell RNA-seq data[23]), and Metabolights database (identifier MTBLS11733). Source data are provided with this paper.

References

1. Loeser, R. F., Goldring, S. R., Scanzello, C. R. & Goldring, M. B. Osteoarthritis: a disease of the joint as an organ. *Arthritis Rheum.* **64**, 1697–1707 (2012).
2. Goldring, M. B., Otero, M., Tsuchimochi, K., Ijiri, K. & Li, Y. Defining the roles of inflammatory and anabolic cytokines in cartilage metabolism. *Ann. Rheum. Dis.* **67**, iii75–iii82 (2008).
3. Hunter, D. J. & Bierma-Zeinstra, S. Osteoarthritis. *Lancet* **393**, 1745–1759 (2019).
4. Wei, G. et al. Risk of metabolic abnormalities in osteoarthritis: a new perspective to understand its pathological mechanisms. *Bone Res.* **11**, 63 (2023).
5. Papathanasiou, I., Anastasopoulou, L. & Tsezou, A. Cholesterol metabolism related genes in osteoarthritis. *Bone* **152**, 116076 (2021).
6. Cho, B. W. et al. Cross-sectional association between hypercholesterolemia and knee pain in the elderly with radiographic knee osteoarthritis: data from the Korean National Health and Nutritional Examination survey. *J. Clin. Med.* **10**, https://doi.org/10.3390/jcm10050933 (2021).
7. Oliviero, F. et al. A comparative study of serum and synovial fluid lipoprotein levels in patients with various arthritides. *Clin. Chim. Acta* **413**, 303–307 (2012).
8. Mishra, R. et al. A comparative analysis of serological parameters and oxidative stress in osteoarthritis and rheumatoid arthritis. *Rheumatol. Int.* **32**, 2377–2382 (2012).
9. Gierman, L. M. et al. Osteoarthritis development is induced by increased dietary cholesterol and can be inhibited by atorvastatin in APOE*3Leiden.CETP mice-a translational model for atherosclerosis. *Ann. Rheum. Dis.* **73**, 921–927 (2014).
10. Cao, C. et al. Cholesterol-induced LRP3 downregulation promotes cartilage degeneration in osteoarthritis by targeting syndecan-4. *Nat. Commun.* **13**, 7139 (2022).
11. Choi, W.-S. et al. The CH25H–CYP7B1–RORα axis of cholesterol metabolism regulates osteoarthritis. *Nature* **566**, 254–258 (2019).
12. Saltiel, A. R. & Olefsky, J. M. Inflammatory mechanisms linking obesity and metabolic disease. *J. Clin. Investig.* **127**, 1–4 (2017).
13. Tall, A. R. & Yvan-Charvet, L. Cholesterol, inflammation and innate immunity. *Nat. Rev. Immunol.* **15**, 104–116 (2015).
14. Robinson, W. H. et al. Low-grade inflammation as a key mediator of the pathogenesis of osteoarthritis. *Nat. Rev. Rheumatol.* **12**, 580–592 (2016).
15. Jenei-Lanzl, Z., Meurer, A. & Zaucke, F. Interleukin-1β signaling in osteoarthritis – chondrocytes in focus. *Cell. Signal.* **53**, 212–223 (2019).
16. Rosenberg, J. H., Rai, V., Dilisio, M. F. & Agrawal, D. K. Damage-associated molecular patterns in the pathogenesis of osteoarthritis: potentially novel therapeutic targets. *Mol. Cell Biochem.* **434**, 171–179 (2017).
17. Kroemer, G. & Reed, J. C. Mitochondrial control of cell death. *Nat. Med.* **6**, 513–519 (2000).
18. Chan, D. C. Mitochondria: dynamic organelles in disease, aging, and development. *Cell* **125**, 1241–1252 (2006).
19. Hopfner, K. P. & Hornung, V. Molecular mechanisms and cellular functions of cGAS-STING signalling. *Nat. Rev. Mol. Cell Biol.* **21**, 501–521 (2020).
20. Brestoff, J. R. et al. Intercellular mitochondria transfer to macrophages regulates white adipose tissue homeostasis and is impaired in obesity. *Cell Metab.* **33**, 270–282.e278 (2021).
21. Levoux, J. et al. Platelets facilitate the wound-healing capability of mesenchymal stem cells by mitochondrial transfer and metabolic reprogramming. *Cell Metab.* **33**, 283–299.e289 (2021).
22. Zhou, H. et al. Osteocyte mitochondria inhibit tumor development via STING-dependent antitumor immunity. *Sci. Adv.* **10**, eadi4298 (2024).
23. Ji, Q. et al. Single-cell RNA-seq analysis reveals the progression of human osteoarthritis. *Ann. Rheum. Dis.* **78**, 100–110 (2019).
24. Zhang, B. C. et al. Cholesterol-binding motifs in STING that control endoplasmic reticulum retention mediate anti-tumoral activity of cholesterol-lowering compounds. *Nat. Commun.* **15**, 2760 (2024).
25. Guo, Q. et al. STING promotes senescence, apoptosis, and extracellular matrix degradation in osteoarthritis via the NF-κB signaling pathway. *Cell Death Dis.* **12**, 13 (2021).

26. Haag, S. M. et al. Targeting STING with covalent small-molecule inhibitors. *Nature* **559**, 269–273 (2018).
27. Lee, G. et al. Enhancement of intracellular cholesterol efflux in chondrocytes leading to alleviation of osteoarthritis progression. *Arthritis Rheumatol.* **77**, 151–162 (2025).
28. Goldring, S. R. & Goldring, M. B. Changes in the osteochondral unit during osteoarthritis: structure, function and cartilage-bone crosstalk. *Nat. Rev. Rheumatol.* **12**, 632–644 (2016).
29. Liao, P. et al. Osteocyte mitochondria regulate angiogenesis of transcortical vessels. *Nat. Commun.* **15**, 2529 (2024).
30. Wrona, A., Balbus, J., Hrydziuszko, O. & Kubica, K. Two-compartment model as a teaching tool for cholesterol homeostasis. *Adv. Physiol. Educ.* **39**, 372–377 (2015).
31. Liu, D. et al. Intercellular mitochondrial transfer as a means of tissue revitalization. *Signal Transduct. Target Ther.* **6**, 65 (2021).
32. Gao, J. et al. Endoplasmic reticulum mediates mitochondrial transfer within the osteocyte dendritic network. *Sci. Adv.* **5**, eaaw7215 (2019).
33. Ikeda, H. et al. Immune evasion through mitochondrial transfer in the tumour microenvironment. *Nature* **638**, 225–236 (2025).
34. Ahmad, T. et al. Miro1 regulates intercellular mitochondrial transport & enhances mesenchymal stem cell rescue efficacy. *Embo J.* **33**, 994–1010 (2014).
35. Mayan, M. D. et al. Articular chondrocyte network mediated by gap junctions: role in metabolic cartilage homeostasis. *Ann. Rheum. Dis.* **74**, 275–284 (2015).
36. Zhang, H., Cai, D. & Bai, X. Macrophages regulate the progression of osteoarthritis. *Osteoarthr. Cartil.* **28**, 555–561 (2020).
37. Chen, Q., Sun, L. & Chen, Z. J. Regulation and function of the cGAS-STING pathway of cytosolic DNA sensing. *Nat. Immunol.* **17**, 1142–1149 (2016).
38. Hu, M. M. & Shu, H. B. Mitochondrial DNA-triggered innate immune response: mechanisms and diseases. *Cell. Mol. Immunol.* **20**, 1403–1412 (2023).
39. Cighetti, G., Del Puppo, M., Paroni, R., Fiorica, E. & Galli Kienle, M. Pantethine inhibits cholesterol and fatty acid syntheses and stimulates carbon dioxide formation in isolated rat hepatocytes. *J. Lipid Res.* **28**, 152–161 (1987).
40. Cighetti, G., Del Puppo, M., Paroni, R. & Galli Kienle, M. Modulation of HMG-CoA reductase activity by pantetheine/pantethine. *Biochim. Biophys. Acta* **963**, 389–393 (1988).
41. Kerr, E. W., Shumar, S. A. & Leonardi, R. Nudt8 is a novel CoA diphosphohydrolase that resides in the mitochondria. *FEBS Lett.* **593**, 1133–1143 (2019).
42. Rumberger, J. A., Napolitano, J., Azumano, I., Kamiya, T. & Evans, M. Pantethine, a derivative of vitamin B(5) used as a nutritional supplement, favorably alters low-density lipoprotein cholesterol metabolism in low- to moderate-cardiovascular risk North American subjects: a triple-blinded placebo and diet-controlled investigation. *Nutr. Res.* **31**, 608–615 (2011).
43. Brunetti, D. et al. Pantethine treatment is effective in recovering the disease phenotype induced by ketogenic diet in a pantothenate kinase-associated neurodegeneration mouse model. *Brain* **137**, 57–68 (2014).
44. Stone, N. J. et al. 2013 ACC/AHA guideline on the treatment of blood cholesterol to reduce atherosclerotic cardiovascular risk in adults: a report of the American College of Cardiology/American Heart Association Task Force on Practice Guidelines. *J. Am. Coll. Cardiol.* **63**, 2889–2934 (2014).
45. Moses, M. A., Sudhalter, J. & Langer, R. Identification of an inhibitor of neovascularization from cartilage. *Science* **248**, 1408–1410 (1990).
46. Grüneboom, A. et al. A network of trans-cortical capillaries as mainstay for blood circulation in long bones. *Nat. Metab.* **1**, 236–250 (2019).
47. Yu, X. H., Zhang, D. W., Zheng, X. L. & Tang, C. K. Cholesterol transport system: an integrated cholesterol transport model involved in atherosclerosis. *Prog. Lipid Res.* **73**, 65–91 (2019).
48. Lai, X. et al. The dependences of osteocyte network on bone compartment, age, and disease. *Bone Res.* **3**, 15009 (2015).
49. Barutta, F. et al. Protective effect of the tunneling nanotube-TNFAIP2/M-sec system on podocyte autophagy in diabetic nephropathy. *Autophagy* **19**, 505–524 (2023).
50. Geiger, O., Sanchez-Flores, A., Padilla-Gomez, J. & Degli Esposti, M. Multiple approaches of cellular metabolism define the bacterial ancestry of mitochondria. *Sci. Adv.* **9**, eadh0066 (2023).
51. Roger, A. J., Muñoz-Gómez, S. A. & Kamikawa, R. The origin and diversification of mitochondria. *Curr. Biol.* **27**, R1177–r1192 (2017).
52. West, A. P., Shadel, G. S. & Ghosh, S. Mitochondria in innate immune responses. *Nat. Rev. Immunol.* **11**, 389–402 (2011).
53. Ding, P. et al. Mitochondria from osteolineage cells regulate myeloid cell-mediated bone resorption. *Nat. Commun.* **15**, 5094 (2024).
54. Stegen, S. et al. HIF-1α metabolically controls collagen synthesis and modification in chondrocytes. *Nature* **565**, 511–515 (2019).
55. Ma, Y. et al. Targeting Parkin-regulated metabolomic change in cartilage in the treatment of osteoarthritis. *iScience* **27**, 110597 (2024).
56. Liu, D. et al. Mitochondrial quality control in cartilage damage and osteoarthritis: new insights and potential therapeutic targets. *Osteoarthr. Cartil.* **30**, 395–405 (2022).
57. Riksen, N. P., Bekkering, S., Mulder, W. J. M. & Netea, M. G. Trained immunity in atherosclerotic cardiovascular disease. *Nat. Rev. Cardiol.* **20**, 799–811 (2023).
58. Chang, X. et al. Pilot trial on the efficacy and safety of pantethine in children with pantothenate kinase-associated neurodegeneration: a single-arm, open-label study. *Orphanet J. Rare Dis.* **15**, 248 (2020).
59. Ryu, K. W. et al. Cellular ATP demand creates metabolically distinct subpopulations of mitochondria. *Nature* **635**, 746–754 (2024).
60. Tan, S. & Kory, N. Divide and conquer, mitochondrial edition: subpopulations direct cellular energy and nutrient supply. *Cell Metab.* **37**, 5–6 (2025).
61. Chen, L. et al. Mitochondrial heterogeneity in diseases. *Signal Transduct. Target Ther.* **8**, 311 (2023).
62. Kavian, N. et al. Pantethine prevents murine systemic sclerosis through the inhibition of microparticle shedding. *Arthritis Rheumatol.* **67**, 1881–1890 (2015).

Acknowledgements

This study was financially supported by the Shanghai Rising-star Program (24QA2706600, Gao, J.), National Key Research and Development Program of China (2023YFC2509600, Qu, X.), Shanghai Frontiers Science Center of Degeneration and Regeneration in Skeletal System (BJ1-9000-22-4002, Zhang, C.), Shanghai 2024 "Science and Technology Innovation Action Plan" Natural Science Fund project application guide (24ZR1456600, Gao, J.), Shanghai Oriental Talent Plan Youth Program (Gao, J.) and National Key R&D Program of China (2024YFA0919200, Gao, J.).

Author contributions

Conceptualization: J.J.G. Methodology: J.J.G., W.T.J., Y.G.H., and D.J.D. Investigation: Y.Y.M., Y.D.P., C.L.L., Y.C.T., M.Y., X.F.L., R.M.C., Z.K.Z, K.W.Z., Y.W.Z., D.Y.Z., and H.P. Visualization: J.J.G., C.Q.Z., and C.J.L. Funding acquisition: J.J.G., C.Q.Z., and X.H.Q. Supervision: J.J.G., C.Q.Z., C.J.L., Y.G.H., and P.Y. Writing–original draft: Y.Y.M., Y.D.P., C.L.L., and Y.C.T. Writing–review and editing: J.J.G., C.Q.Z., Y.G.H., and P.Y.

Competing interests

The authors declare no competing interests.

Additional information

Supplementary information The online version contains supplementary material available at https://doi.org/10.1038/s41467-025-65689-w.

Correspondence and requests for materials should be addressed to Pei Yang, Yigang Huang, Changqing Zhang or Junjie Gao.

Peer review information *Nature Communications* thanks Jin Cheng and the other anonymous reviewer(s) for their contribution to the peer review of this work. A peer review file is available.

Reprints and permissions information is available at http://www.nature.com/reprints